The evolution of El Niño-Southern Oscillation amplitude asymmetry since the Last Glacial Maximum

Zhengyao Lu[1,2], Matthieu Carré[3], Chris Brierley[4], Anna Schultze[2], Peter O. Hopcroft[5], Kewei Lyu[1], Debo Zhao[6], Minjie Zheng[7,2], Pascale Braconnot[8], Qiuzhen Yin[9], Johann H. Jungclaus[10], Xiaoxu Shi[11], Birgit Schneider[12], Haijun Yang[13], Qiong Zhang[14]

[1] *College of Ocean and Earth Sciences, Xiamen University, Xiamen, China*

[2] *Department of Earth and Environmental Sciences, Lund University, Lund, Sweden*

[3] *IPSL/Laboratoire des Sciences du Climat et de l'Environnement (LSCE UMR8212 CEA, CNRS, UVSQ), Gif sur Yvette, France*

[4] *Department of Geography, University College London, London, United Kingdom*

[5] *School of Geography, Earth & Environmental Sciences, University of Birmingham, United Kingdom*

[6] *Key Laboratory of Ocean Observation and Forecasting, Laboratory of Marine Geology and Environment, Institute of Oceanology, Chinese Academy of Sciences, Qingdao, China*

[7] *Laboratory for Humid Subtropical Ecogeographical Processes of the Ministry of Education, School of Geographical Sciences, Fujian Normal University, Fuzhou, China*

[8] *Laboratoire des Sciences du Climat et de l'Environnement, LSCE/IPSL, CEA-CNRS-UVSQ, Université Paris-Saclay, Gif-sur-Yvette, France*

[9] *Earth and Climate Research Center, Earth and Life Institute, Université catholique de Louvain, Louvain-la-Neuve, Belgium*

[10] *Max Planck Institut für Meteorologie, Hamburg, Germany*

[11] *Southern Marine Science and Engineering Guangdong Laboratory (Zhuhai), Zhuhai, China*

[12] *Christian-Albrechts-Universität zu Kiel, Kiel, Germany*

[13] *Department of Atmospheric and Oceanic Sciences, Fudan University, Shanghai, China*

[14] *Department of Physical Geography and Bolin Centre for Climate Research, Stockholm University, Stockholm, Sweden*

Corresponding author: Zhengyao Lu (zhengyao.lu@xmu.edu.cn)

Abstract

El Niño-Southern Oscillation (ENSO) amplitude asymmetry—the preferential amplification of El Niño relative to La Niña—is a defining expression of tropical climate nonlinearity and a key determinant of global hydroclimate extremes. Yet its long-term evolution and stability under radically different climate states remain poorly constrained. Here we reconstruct ENSO amplitude asymmetry since the Last Glacial Maximum (~21,000 years ago) using a synthesis of tropical Pacific sea-surface temperature (SST), SST anomaly (SSTA) and thermocline temperature skewness derived from fossil corals, mollusk shells and individual foraminifera, combined with transient coupled climate simulations. We show that ENSO skewness increased progressively through the Holocene, driven primarily by amplification of El Niño relative to La Niña, consistent with orbitally forced shoaling of the equatorial thermocline. In contrast, millennial-scale perturbations during Heinrich Stadial 1, the Bølling-Allerød and the Younger Dryas produced abrupt, non-monotonic skewness changes associated with reorganisations of ENSO spatial structure linked to Atlantic Meridional Overturning Circulation (AMOC) variability. By establishing SST skewness as a robust paleoclimate diagnostic of ENSO nonlinearity, our findings provide a critical long-term perspective on its stability, revealing its sensitivity to mean-state changes and offering a framework to reduce uncertainty in future ENSO projections.

1. Introduction

ENSO is the Earth's major mode of interannual climate variability[1], fundamentally defined by its inherent nonlinearity[2] and the resulting asymmetry in amplitude between its warm (El Niño) and cold (La Niña) phases[3]. Extreme El Niño events routinely achieve magnitudes far greater than the strongest La Niña events[4], triggering even more disproportionate socio-economic[5,6] and ecological[7] catastrophes. While La Niña events are typically weaker in amplitude, their impacts are often exacerbated by a greater potential for long-duration events[8,9], which can lead to cumulative damages from prolonged droughts and flooding across the Pacific Rim[10]. Beyond these direct impacts, amplitude asymmetry serves as a critical indicator of climate model realism, as it is frequently used as an emergent constraint to narrow the uncertainty and spread of future ENSO projections[9,11,12].

Observations indicate that ENSO amplitude as well as the atmospheric convective nonlinearity (in the climatologically cold eastern Pacific, convection responds more sensitively to warm than cold SSTA) asymmetry strengthened during the 20th century[13,14]. However, the trajectory of this asymmetry under greenhouse warming is likely non-monotonic and sensitive to both mean-state changes and internal variability. Under transient greenhouse warming through the end of the 21st century, ENSO is projected to be more extreme, potentially accompanied by an intensification of its asymmetric characteristics[15]. Intriguingly, recent studies report a substantial weakening of both ENSO amplitude and its asymmetry post-2100 under persistent, high-emission greenhouse warming scenarios[16-18]. This reversal suggests that the nonlinear behavior of ENSO is not a static feature but one that evolves drastically as the background climate state shifts.

The physical basis of this asymmetry is an intricate interplay of coupled nonlinearities in both the atmosphere and ocean[3,19]. The nonlinear atmospheric convective feedback and equatorial zonal wind stress response to SST forcing are identified as major contributing atmospheric processes[20-23]. This is bolstered by state-dependent stochastic forcing from Westerly Wind Bursts, which are more likely to occur as the warm pool expands eastward associated with the warm events[24-26]. Oceanic dynamics shape and amplify these initial atmospheric signals through processes such as nonlinear temperature advection[27,28], tropical instability waves[29,30], thermocline depth-modulated ENSO feedbacks[31,32], and subsurface nonlinear dynamical heating[33], all of which favor the warm tail of the distribution[34]. Because the sensitivity of most suggested mechanisms is intrinsically linked to the mean climate, investigating their behavior across the radical state changes of the geological past[35] is essential for verifying their robustness.

In paleoclimatology, while changes in overall ENSO amplitude have been documented relatively well across various epochs, e.g.[36-43], investigations into amplitude asymmetry[37,44] remain notably limited. This gap is primarily due to a historical lack of high-resolution, continuous proxy data capable of tracking individual interannual events and the higher-order nonlinearity statistics over millennial or longer timescales.

To address this, we reconstruct the history of ENSO amplitude asymmetry since the Last Glacial Maximum (LGM), approximately 21,000 years ago[45]. We develop a synthesis of diverse varying-resolution paleoclimate proxies—specifically integrating SST/SST anomaly (SSTA) and thermocline temperature skewness signatures from fossil coral, mollusk shells and individual foraminifera preserved in marine sediments located within the tropical central and eastern Pacific—with a group of transient non-accelerated global climate model simulations collectively spanning this period. By blending geochemical records with continuous simulations, we reveal ENSO's asymmetric evolution and identify the mechanisms driving it across different boundary conditions.

2. Results

2.1 ENSO control of upper ocean temperature skewness in observations

We begin by assessing the extent to which SST and thermocline temperature skewness—a metric that can be obtained from corals, mollusks, and individual foraminifera proxies—reflects ENSO asymmetry in the modern climate using the ERSST v5[46] and ORA5[47] reanalysis. Skewness, the third moment of SSTA distribution, provides a direct statistical measure of ENSO amplitude asymmetry[48] (Methods). Interannual SSTA in the tropical Pacific are approximately Gaussian, and positively skewed as El Niño events expand the warm tail of the distribution (Fig. S1a,c). As such, SSTA skewness has been widely used to characterize ENSO nonlinearity in observations and models. In this regard, the distribution of SSTA skewness exhibits a pronounced zonal gradient across the tropical Pacific, with increasingly positive values toward the ENSO action center in the eastern equatorial Pacific (Fig. 1a). This pattern closely follows the spatial footprint of ENSO variability, indicating that ENSO dynamics dominate higher-order SST statistics on interannual timescales. Sensitivity experiments in which ENSO amplitudes during identified events are artificially scaled by ±50% (Methods) further confirm that the SSTA skewness response is spatially coherent and nearly basin-wide (Fig. 1e,f; Fig. S2a-h, blue lines), demonstrating that ENSO amplitude overwhelmingly controls the SSTA skewness signal across the tropical Pacific.

The interpretation of SST skewness is less straightforward, as SST variability integrates interannual anomalies with the seasonal cycle and mean-state variability. Climatologically, SST skewness nonetheless displays a systematic east-west gradient similar to that of SSTA skewness (Fig. 1b). Tropical Pacific SST distributions can be approximated as a superposition of a quasisinusoidal seasonal cycle and a Gaussian interannual component associated with ENSO (Fig. S1b,d), particularly towards the eastern side of the basin with more pronounced annual cycle of SST[49,50] (Fig. S1d). The interaction between these components determines the net SST skewness.

Despite this complexity, asymmetric ENSO amplitude perturbations produce a distinct and physically consistent SST skewness response. The equatorial central Pacific exhibits more positive (negative) SST & SSTA skewness under enhanced El Niño (La Niña) amplitudes (Fig. 1c-f; Fig. S2a-h, red lines), and less sensitive to the seasonal cycle amplitude (Fig. S2d,h). This sensitivity extends eastward to the coastal eastern Pacific, and further into the coastal ocean along Central and South America, delineating a coherent ENSO-driven imprint on the full SST distribution. Regional diagnostics corroborate these spatial patterns (Fig. S2a-h), and further show that both SST and SSTA skewness vary monotonically with ENSO amplitude across perturbations ranging from ±10% to ±60%, with comparable magnitudes of response for El Niño and La Niña.

While the Niño 1+2 region is more strongly influenced by the seasonal cycle and remote subtropical variability[49,51,52] (Fig. 1c,d; Fig. S2e,f vs. a,b), this does not preclude its usefulness for diagnosing ENSO amplitude asymmetry using SST skewness. Notably, both SST and SSTA skewness increase monotonically with ENSO amplitude toward the easternmost extent of ENSO's influence, supporting the robustness of this metric in that region. Interestingly, thermocline temperature skewness exhibits an even stronger sensitivity to ENSO amplitude modulation, particularly in the Niño 1+2 region, suggesting that it may provide a more robust proxy for ENSO asymmetry than SST skewness (Fig. S2i-p; Fig. S3).

Together, these results establish that both SSTA and thermocline temperature skewness provide basin-wide diagnostics of ENSO asymmetry, while SST skewness more robustly reflects ENSO nonlinearity in the equatorial central Pacific and along the American margins. These regions therefore constitute optimal targets for reconstructing the long-term evolution of ENSO asymmetry using SST- and thermocline temperature-based paleoclimate records.

2.2 The evolution of ENSO skewness since the Last Glacial Maximum

2.2.1 Proxy-based reconstructions

Proxy temperature-based reconstructions of ENSO skewness (Methods) remain inherently noisy (Fig. 2), reflecting both its stochastic nature[13] and limitations in sampling resolution, record length (short segments can be strongly influenced by individual extreme events; Fig. S4), site distribution (Fig. 1b markers), and other sources of uncertainties (Methods). Nevertheless, when considered collectively, robust and coherent long-term trends emerge, particularly over the Holocene, across both the central and eastern equatorial Pacific and across all proxy types analysed.

In the central equatorial Pacific, monthly-resolved fossil corals and an ocean sediment record consistently indicate a progressive increase in skewness, on the order of 0.07-0.11 per thousand years (ka) over the last ~10 ka, implying a robust strengthening of ENSO amplitude asymmetry through the Holocene (Fig. 2a; Fig. S5). A similar signal emerges from the proxy cluster in the eastern equatorial Pacific, where mollusk shell records and several independent ocean sedimentary archives also indicate an increasing skewness trend throughout the Holocene (Fig. 2b,c). The magnitude of the trend is comparable to that inferred for the central Pacific, with estimated increases of 0.02-0.06 per ka over the last ~10 ka.

Comparison between the two cluster regions reveals that the Holocene increase in skewness is not contingent on shifts between Central Pacific (CP) and Eastern Pacific (EP) El Niño spatial patterns. Both regions exhibit coherent increases despite their opposite sensitivities to ENSO flavors (Fig. S6), implying that the evolving asymmetry reflects a basin-wide intensification of ENSO nonlinearity, rather than a sole redistribution of El Niño activity between CP and EP modes[53].

Prior to the Holocene, the deglacial evolution of SST skewness presents a more complex picture. In the central equatorial Pacific, only three data points are available; these suggest that skewness during the LGM was comparable to that of the late Holocene, implying substantial ENSO asymmetry even under glacial boundary conditions (Fig. 2a). In the eastern equatorial Pacific, a larger suite of sediment records captures pronounced skewness variability (Fig. 2b,c). During the early deglaciation, skewness remains in a positive state comparable to the late Holocene, then gradually weakens before exhibiting large millennial-scale fluctuations across Heinrich Stadial 1 (HS1), the Bølling-Allerød (BA), and the Younger Dryas (YD). Several records show particularly elevated skewness around the BA, exceeding the late-Holocene values and indicating transient episodes of enhanced ENSO asymmetry superimposed on the longer-term deglacial trend.

2.2.2 Transient climate model simulations

We compare these reconstructions with transient global climate model simulations spanning the LGM to the present. During the Holocene, four selected models (out of nine available; Methods) show a consistent increase in SST and SSTA skewness over the last ~7 ka in both the CP and EP (in Niño 3.4 and Niño 1+2 regions, respectively; Fig. 3a-d), in agreement with the proxy synthesis. Although the magnitude of SST skewness varies across models (~0.05 per ka in Niño 3.4 and (~0.014 per ka Niño 1+2), the sign and temporal evolution are robust, supporting an orbitally forced origin for the Holocene trend.

For the deglaciation, only one transient simulation (iTRACE[54]; Methods) is currently available. This simulation exhibits a distinct evolution (Fig. 3a-d): SST skewness decreases from the LGM to a minimum at ~16 ka, then increases abruptly to a peak near ~13.5 ka, before declining again toward another trough at ~12 ka, and then rebounds towards the early Holocene. This transient pulse is present in both the CP and EP. The latter broadly mirrors the proxy-inferred variability, with indications of enhanced skewness around the BA interval. The similarity between SSTA and SST skewness evolution, particularly in the CP, supports a shared ENSO-related control on both measures.

Overall, the data-model comparison indicates that the large-scale evolution of ENSO skewness since the LGM is reproducible in transient simulations, lending confidence to both the proxy interpretation and the underlying physical mechanisms.

2.3 Representation of ENSO amplitude in SST skewness

To understand the reconstructed skewness changes, we examine separately the evolution of El Niño and La Niña amplitudes (Methods) and comparing their relative strength in both proxy records and transient climate simulations.

During the Holocene, the increase in SST skewness is primarily driven by an amplification of El Niño events. The CP fossil coral records indicate a systematic increase in El Niño amplitude, while La Niña amplitude exhibits no clear long-term trend within proxy uncertainty (Fig. 3f; Fig. S7). We use the simulated Niño 3 index to provide a balanced representation of ENSO activity for both CP and EP events. This asymmetry is broadly reproduced in the multi-model ensemble mean, which shows a robust intensification of El Niño alongside a slightly more moderate increase in La Niña amplitude (Fig. 3f). Consequently, the El Niño-to-La Niña amplitude ratio increases through the Holocene (Fig. 3e), reflecting progressively more positive SST/SSTA skewness. Accordingly, the minimum in reconstructed skewness at the early/mid-Holocene corresponds to a state in which both El Niño and La Niña are extensively weakened, and their amplitude ratio approaches equality. It should be noted that given the inherent nonlinearity of coupled ocean-atmosphere feedbacks that preferentially amplify warm SSTA over cold SSTA, it is dynamically unlikely, even over the orbital timescales, that La Niña systematically exceeds El Niño in amplitude (Fig. 3f).

Over the deglaciation, direct estimate on phase-dependent ENSO amplitude is limited to iTRACE simulation (Fig. 3e,f). In the early deglacial interval, both El Niño and La Niña amplitudes decline gradually, with a stronger reduction in El Niño, which mirrors the late Holocene, leading to a decrease in skewness. However, during the millennial-scale variability associated with HS1, BA, and YD, the relationship between amplitude and skewness becomes markedly non-monotonic. During the BA, ENSO amplitude in both phases weakens while skewness increases sharply, reaching a maximum over the 20-12 ka interval; this peak is bracketed by preceding and subsequent declines in skewness during the HS1 and YD, accompanied with strengthened El Niño and La Niña amplitudes.

This decoupling, particularly during periods of abrupt climate change, reveals that ENSO skewness is not always positively correlated with the magnitude of its El Niño phase, or simply determined by extreme El Niño events. It suggests a shift in the governing mechanisms for ENSO asymmetry evolution since the LGM, with slow orbital precession forcing exerting coherent control over the Holocene and early deglaciation. This precessional forcing, varying on ~21,000-year timescales, is closely tracked by the evolution of ENSO asymmetry; in contrast, millennial-scale perturbations reorganize nonlinear feedbacks that differentially regulate El Niño and La Niña growth through other processes (detailed below).

2.4 Forcing mechanisms and dynamical interpretation

Indeed, our results suggest that ENSO asymmetry is governed by distinct mechanisms on these orbital and millennial timescales. During the Holocene and the early deglaciation, the coherent evolution of SST skewness and El Niño-La Niña amplitude ratios points to a dominant role for slow modulation of the tropical Pacific mean state, particularly zonal temperature contrast, thermocline depth and stratification[55], driven by precessional forcing (Fig. 4). Seasonal insolation changes associated with precession (Fig. 4a) generate weakened zonal SST gradient and a shift from La Niña-like to El Niño-like state across the Holocene[56] (Fig. 4e). This process, combined with weakened Walker circulation, and reinforced by SST anomalies in the extratropical South Pacific that propagate equatorward and downward[55,57], imprinting a precession-scale signal on the equatorial thermocline. In the tropical central and western Pacific, both proxy[58-60] and model simulations (Fig. 4f) indicate a progressively shallower thermocline toward the late Holocene and during the early deglaciation towards the LGM. The oceanic wave response to wind stress depends strongly on background stratification, and hence such shoaling of thermocline changes can enhance the sensitivity of equatorial Rossby waves to wind stress curl preferentially amplify El Niño relative to La Niña, leading to systematic amplitude asymmetry[30,31]. This mechanism provides a physically consistent explanation for the monotonic increase in skewness driven primarily by El Niño amplification over the precessional timescale.

During the early deglaciation, the evolution of ENSO skewness remains consistent with the orbital-scale mechanism identified for the Holocene. Here, iTRACE shows a gradual weakening of both El Niño and La Niña amplitudes, with a stronger reduction in El Niño, leading to reduced skewness (Fig. 3e,f). This behavior is consistent with slow precessional modulation of the tropical Pacific mean state and thermocline structure (Fig. 4a,e,f).

In contrast, the pronounced millennial-scale pulses in skewness during the HS1, BA and YD reflect a distinct mechanism linked to meltwater-forced AMOC variability. Freshwater discharge into the North Atlantic during HS1 leads to a substantially weakened AMOC (Fig. 4b). ENSO amplitude and diversity response to AMOC strength has been widely reported in previous studies[61-63] (Fig. 4d). In iTRACE, this background state is associated with an eastward displacement of both CP and EP El Niño centers (Fig. S8), resulting in a zonal shift in the distributions of SST and SSTA skewness (Fig. S9). In particular, the closer distance between the center of CP and EP El Niño due to their zonal propagation (Fig. 4f, black line) suggests weakened ENSO diversity and nonlinearity[14,19,64], and thus reduced ENSO asymmetry (Fig. 4c). This is consistent with the El Niño to La Niña amplitude ratio decrease (Fig. 3e) associated with reduced skewness, even though ENSO variance increases during HS1 and YD (Fig. 4d), with strengthened El Niño and La Niña amplitudes (Fig. 3f). Conversely, during the BA, AMOC recovery and overshoot reverse these patterns, as indicated by a westward shift of CP and EP El Niño centers and longer distance between the two centers (Fig. 4f; Fig. S8), and thus stronger ENSO diversity and nonlinearity, accompanied by weakened ENSO amplitude (Fig. 4d) but an increased El Niño to La Niña amplitude ratio (Fig. 3e), resulting in peak skewness in Niño 3 (Fig. 4c). Alternatively, abrupt H1 and YD cooling can suppress tropical convections, as deep convection thresholds become more difficult to reach in the eastern Pacific, and the development of strong eastern Pacific El Niño events is inhibited[15], reducing SST skewness despite an overall increase in ENSO variability. Beyond these AMOC-driven dynamics, the massive retreat and melt of continental ice sheets during the deglaciation and into the early Holocene may have exerted forcing that enhanced ENSO activity[65,66] and influenced ENSO asymmetry. Yet, this intensification was likely counterbalanced by the concomitant rise in atmospheric CO2, which simultaneously drives a weakening of ENSO[55,67], thereby resulting in a muted net signal.

Together, these results indicate that ENSO skewness during the deglaciation reflects a superposition of slow orbital modulation of background asymmetry and rapid, event-driven reorganisation of El Niño spatial structure during meltwater perturbations. The consistent behavior across proxy records and model simulations supports this dual control and underscores the sensitivity of ENSO asymmetry to both gradual mean-state evolution and abrupt circulation changes.

3. Summary and discussion

Our synthesis demonstrates that the tropical Pacific SST skewness provides a dynamically robust measure of ENSO asymmetry since the LGM, and it reflects how nonlinear amplification of El Niño relative to La Niña interacts with the evolving tropical Pacific mean state. On orbital timescales, ENSO asymmetry increases coherently through the Holocene in both proxy reconstructions and transient simulations. This trend is primarily driven by progressive strengthening of El Niño amplitude relative to La Niña. The consistency across central and eastern Pacific records indicates basin-wide modulation rather than a redistribution between ENSO flavors. The mechanism is consistent with precession-driven adjustment of equatorial thermocline depth and stratification, which alters the efficiency of wind-driven oceanic wave feedbacks and preferentially enhances El Niño growth. ENSO skewness thus emerges as a slow, thermocline-mediated response to orbital forcing. The persistence of substantial skewness during the LGM comparable to the late Holocene conditions further indicates that strong ENSO asymmetry is a resilient feature of the coupled system in the tropical Pacific under boundary conditions very different from today. In contrast, millennial-scale skewness variability during HS1, BA and YD reflects a rapid reorganisation of ENSO spatial structure associated with meltwater-driven perturbations of AMOC. During these events, skewness exhibits transient pulses that are decoupled from overall ENSO variance. Transient simulations indicate systematic east-west shifts of CP and EP El Niño centers, producing distinct skewness responses across the basin. ENSO asymmetry on millennial timescales therefore reflects changes in spatial pattern and diversity, rather than uniform amplitude scaling.

The future evolution of ENSO amplitude asymmetry underscores the complexity of global climate projections. Potential shifts in the frequency and character of ENSO extremes by the end of the twenty-first century carry profound global implications, as they shape the intensity of hydroclimate teleconnections and the magnitude of associated hazards. The SST and thermocline temperature skewness framework developed here offers a powerful new lens through which existing temperature-based reconstructions can be re-examined, with an explicit focus on ENSO amplitude asymmetry in the geological past—particularly during warmer climate states that may serve as analogues for future conditions, such as the Pliocene[68,69]. Expanding coordinated long-duration transient GCM experiments across model ensembles for such constraints would therefore provide a critical pathway to help reduce systematic model biases of ENSO variability and strengthen confidence in projections of future extremes, ensuring that adaptation planning and early-warning strategies are grounded in a more complete understanding of Earth's nonlinear climate dynamics.

Methods

1. Statistical estimation of SST/SSTA skewness via Kernel Density Resampling

To characterize ENSO amplitude asymmetry, we utilise statistical skewness[48] for monthly SST/SSTA and thermocline sea temperature (anomaly) data. Skewness provides a normalised measure that accounts for the entire anomaly distribution regardless of variance. The skewness of distribution is defined as

$$s = \frac{E(x-\mu)^2}{\sigma^3},$$

where μ is the mean of x, σ is the standard deviation of x, and $E(t)$ represents the expected value of the quantity t.

To address the inherent noise in calculating skewness from limited sample sizes, we employ a non-parametric Kernel Density Estimation (KDE) and resampling framework. This approach models the underlying probability density function (PDF) of the limited samples as a continuous distribution. From this estimated smooth distribution, we generated a synthetic N = 1,000,000 data points used for approximating its skewness than direct computation from sparse original data points. Hence, this kernel-based resampling mitigates the influence of limited sample size and individual extremes (Fig. S1).

—

2. Sensitivity of SST/SSTA and thermocline temperature skewness to ENSO amplitude

To assess how SST and SSTA skewness respond to changes in ENSO amplitude, we first identified El Niño and La Niña events in ERSST v5 reanalysis[46] of 1854-2025 (the procedure is described below in *El Niño and La Niña amplitude metrics*). For each event, the associated SST & SSTA pattern was extracted. A series of perturbed anomaly fields were then constructed by scaling identified ENSO SSTA values by ±10%, ±20%, …, up to ±60%. For each scaling factor, the perturbed SSTA values were used directly to compute SSTA skewness (Fig. S2a-c & e-g, blue line). Then, the perturbed SSTA values were added back to the climatological seasonal cycle to reconstruct perturbed full SST fields for skewness (Fig. S2a-c & e-g, red line). This test clearly shows the monotonic relationship between ENSO amplitude and both SST and SSTA skewness in the tropical Pacific. In contrast, seasonal cycle amplitude perturbations exert a weaker influence on skewness (Fig. S2d,h), implying that this seasonal signal—often mixed with interannual SST variability across different background states in paleo ENSO records and simulations (e.g.[70])—does not introduce major biases into skewness interpretations.

Similarly, to evaluate the applicability of thermocline-based proxies for ENSO asymmetry reconstruction, we conducted equivalent sensitivity tests using thermocline temperature and thermocline temperature anomalies in ORA5 reanalysis[47] of 1958-2025 (~50m depth for Niño 1+2 region, ~100m depth for Niño 3.4 region). The results are given in Fig. S2i-j and Fig. S3. These tests show that thermocline temperature skewness exhibits a similarly monotonic response to ENSO amplitude changes, thereby verifying the robustness of subsurface proxy records for reconstructing ENSO asymmetry.

—

3. Proxy synthesis

To capture the SST/SSTA and thermocline temperature skewness to represent statistical distribution of ENSO amplitude asymmetry across different climate states, we synthesised varying-resolution paleoclimate records from three distinct archives: fossil corals, marine mollusks, and individual foraminifera (Supplementary Table 1). These proxies provide the sub-annual resolution necessary to resolve interannual extremes and calculate higher-order moments such as asymmetry and variance.

Central Pacific Fossil Coral Records

We synthesised fossil coral monthly resolved oxygen isotope δ^{18}O data collected from Kiritimati and Fanning Atolls[36,71-73], a region within Niño 3.4 and ideal to record ENSO activity. In total the synthesis covers ~1200 years out of the last ~7 ka. Coral δ^{18}O values reflect a combination of SST and the isotopic composition of seawater, the latter of which is linearly related to sea-surface salinity (SSS). During El Niño (La Niña) events, this region experiences warmer and wetter (cooler and drier) conditions, resulting in negative (positive) coral δ^{18}O anomalies.

Eastern Pacific Mollusk Records

We integrated monthly resolved SST reconstructions derived from fossil *Mesodesma donacium* mollusk shells from coastal Peru[37]. *M. donacium* is a fast-growing aragonitic bivalve with a 1-4 years lifespan that faithfully records environmental conditions at approximately monthly resolution through its growth increments. Because coastal Peru is characterised by extremely arid conditions and minimal river discharge, δ^{18}Osw variations are negligible, allowing shell δ^{18}O to act as a nearly pure temperature proxy. SST values were reconstructed using the aragonite paleotemperature equation from Grossman and Ku (1986)[74]. By aggregating random samples of shells from dated archaeological mounds, we reconstructed the frequency distribution of SST for centennial intervals, providing estimates of past amplitude asymmetry[37].

Individual Foraminiferal Analysis (IFA) of marine sediments

To extend the record to the LGM, we utilised Individual Foraminiferal Analysis (IFA) data from marine sediment cores in the eastern and central equatorial Pacific[40,42,56,75-77]. Planktonic foraminifera, such as *Globigerinoides ruber* (surface-dwelling) and *Neogloboquadrina dutertrei* (thermocline-dwelling), have lifespans of approximately 2-4 weeks. While traditional "bulk" analysis pools a group of shells to estimate mean conditions, IFA measures the geochemistry of individual shells, each representing a monthly "snapshot" of the ocean state. We used reconstructed past SST or thermocline temperature skewness distributions from either δ^{18}O or Magnesium/Calcium (Mg/Ca) ratios from individual records. The Mg/Ca ratio in foraminiferal calcite is exponentially related to the calcification temperature[78]. On the other hand, El Niño events typically bring both warmer temperatures and increased precipitation to the Central/Eastern Pacific, both of which drive δ^{18}O of foraminiferal calcite toward more negative values (e.g. [56]). By analyzing the distribution of these snapshots within a single sediment layer (representing centuries to millennia of accumulation), we identified shifts in the skewness of the temperature distribution, allowing for the detection of changes in ENSO amplitude asymmetry across different background states.

—

4. Global climate model (GCM) transient simulations and model selection

For the Holocene epoch, we analyse transient simulations from the Holocene intercomparison project, contributed by nine research groups worldwide (Supplementary Table 2). Except for TRACE, these simulations were initialised from early- to mid-Holocene boundary conditions (ranging from ~10 to 6 ka; either equilibrium or transient states) and integrated forward to the preindustrial (PI) or present day. The primary external forcing is the evolving seasonal and latitudinal distribution of insolation associated with orbital precession and obliquity[79,80] (e.g., Fig. 4e,j).

For the deglaciation, we analyse the isotope-enabled Transient Climate Evolution experiment (iTRACE)[54] to investigate the mechanisms driving deglacial climate change during 20-11 ka. iTRACE considers a combination of external forcings including evolving ice sheets, greenhouse gas concentrations, orbital insolation, and meltwater fluxes. It is conducted with the isotope-enabled Community Earth System Model, iCESM1.3.

Monthly mean climate variables, including SST and surface air temperature (SAT), are extracted from each simulation. All outputs are regridded to a common 1° × 1° horizontal resolution prior to analysis.

Because our analysis focuses on ENSO skewness and amplitude asymmetry, we evaluate model performance based on their ability to reproduce the observed spatial structure of tropical Pacific SSTA skewness (Fig. S10 & S11). For each simulation, SST anomalies are calculated relative to the model's own climatology, and skewness is computed gridcellwise over the tropical Pacific (20°S-20°N) using the final 100 years of each transient run to approximate near-modern conditions (for iTRACE, the 400-yr data of a pre-Industrial iCESM simulation[81]). The modeled skewness pattern is compared with that derived from ~100 years of observational SST data from the Extended Reconstructed Sea Surface Temperature (ERSST) by a spatial correlation. We select four models[82-85] (out of nine; Supplementary Table 2) that exhibit the highest spatial correlations with ERSST, thereby ensuring that subsequent analyses are based on simulations that most realistically reproduce the observed distribution of ENSO asymmetry.

—

5. Quantifying uncertainty in skewness estimates due to sample size, seasonal bias, and depth habitat

To assess the sensitivity of skewness estimates to sample size, we conducted a subsampling experiment using a synthetic "truth" distribution representative of ENSO skewness derived from ERSST v5 reanalysis. From the full monthly dataset (1854-2025; 2064 total months), we repeatedly drew random subsamples with sizes comparable to those of proxy records (e.g., 30 and 60 samples, Fig. S3). Skewness was calculated for each subsample, and the spread (standard deviation; shown as errorbars in Fig. 2) across 10,000 repeated realisations was used to quantify uncertainty arising from limited sample size.

In addition to sampling uncertainty, we evaluated the potential influence of seasonal and depth-related biases on foraminifera-based skewness estimates using temperature fields from the Holocene transient simulations. Seasonal biases may arise because planktonic foraminifera preferentially record conditions during specific times of the year[86,87], while depth-related biases reflect the fact that different species calcify at varying depths (see "*Proxy synthesis*" in Methods), potentially integrating signals from both surface and subsurface waters.

To test these effects, we calculated skewness under a range of idealised sampling conditions, including seasonally restricted surface temperature (T) and subsurface temperature (Tsub) fields (Fig. S12 & S13; Note in Fig. S13 only EC-Earth results due to data availability). The results indicate that the reconstructed evolution of skewness is robust to these factors: an increasing trend in SST skewness across the Holocene is evident even when sampling is limited to specific seasons, and similar behavior is obtained when using subsurface temperatures alone.

Importantly, in the tropical eastern Pacific, subsurface planktonic foraminifera can track ENSO-induced wind forcing and large-scale thermal gradients more effectively than surface species (Fig. S2 a-h vs. i-p), as sea surface temperatures (SST) are inherently confounded by localised dynamic and thermodynamic factors.

Together, these sensitivity tests suggest that neither seasonal nor depth-related biases fundamentally alter the inferred ENSO asymmetry signal at orbital timescales, supporting the use of mixed surface- and subsurface-dwelling foraminiferal records to reconstruct skewness.

—

6. El Niño and La Niña amplitude metrics

El Niño and La Niña events were identified from monthly SST anomalies in the Niño 3 region (5°S-5°N, 170°W-120°W) following standard criteria: an event is initiated when the three-month running mean SSTA exceeds +0.5 °C for El Niño or falls below -0.5 °C for La Niña and persists for at least five overlapping months. For each identified event, the amplitude of El Niño or La Niña was defined as the average SSTA over all active months (i.e., months meeting event criteria). These amplitudes were aggregated across events within a given temporal bin (e.g., 100-year model window or time interval of 1 coral slice, within which the mean seasonal cycle and SSTA were calculated) to compute ensemble mean amplitudes for each phase, enabling comparison between phases and across time.

—

7. Identification of CP vs EP El Niño

We distinguished between CP and EP El Niño types in iTRACE and ERA5 reanalysis using the Empirical Orthogonal Function (EOF) decomposition and rotation method proposed by Takahashi et al.[88]. The first two principal modes PC_1 and PC_2 were derived from the eigendecomposition of the temporal covariance matrix of monthly SSTA. To isolate the geographically distinct warming centers, the PCs were rotated by 45° to produce the E (Eastern) index and C (Central) index:

$$E = \frac{PC_1 - PC_2}{\sqrt{2}},\ C = \frac{PC_1 + PC_2}{\sqrt{2}}$$

The spatial centers of action for each flavor are identified through grid-wise linear regression. We regress the original SSTA field onto the standardised E and C indices. The resulting regression coefficients represent the spatial patterns of the two modes (Fig. S8a,b). EP and CP El Niño events can be identified using a 0.5°C threshold for 3-month running mean E and C indices for five consecutive months and is classified as EP (CP) El Niño if the E index exceeds C index (C index exceeds E index) during the peak phase.

Figures

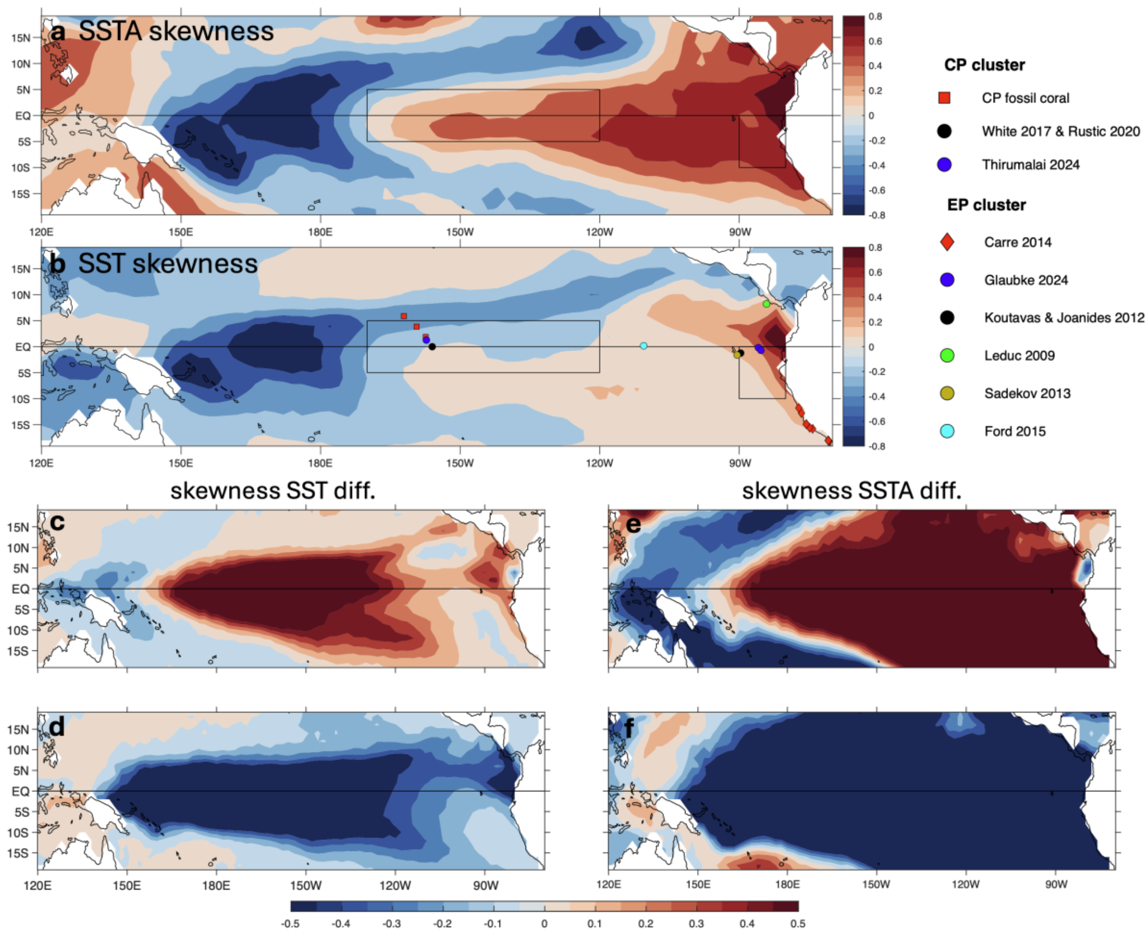

Figure 1 | Spatial patterns and sensitivity of tropical Pacific SST/SSTA skewness. a, b, Spatial distribution of (**a**) SSTA skewness and (**b**) SST skewness across the tropical Pacific (1854-2025). Black boxes denote Niño 3.4 (5°S-5°N, 170-120°W) and Niño 1+2 regions (10°S-0°N, 90-80°W). In **b**, markers indicate the geographic locations of all proxy reconstructions used in this study. **c-f**, Sensitivity of skewness to ENSO intensity. Maps show the projected response of (**c, d**) SST skewness and (**e, f**) SSTA skewness under idealised conditions in which all identified (**c, e**) El Niño and (**d, f**) La Niña event amplitudes are artificially amplified and reduced by 50% and their skewness differences are calculated, which is applied to all gridcells (Methods).

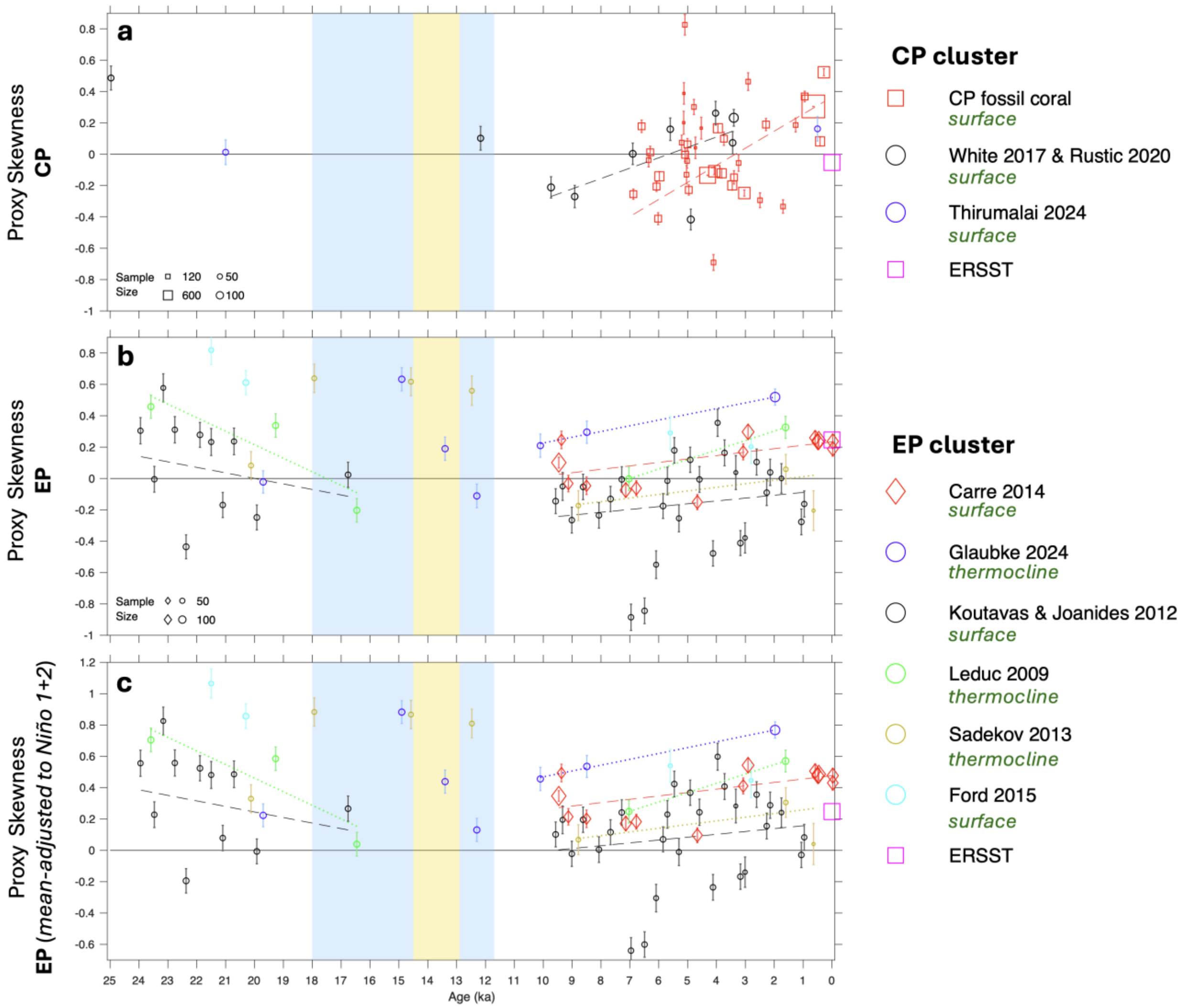

Figure 2 | Reconstructed SST skewness from proxy records since the LGM. a, Evolution of reconstructed SST skewness from the Central Pacific (CP cluster). **b**, same as **a**, but for SST or thermocline temperature skewness from the Eastern Pacific (EP cluster). Note that in **b** the records cannot be directly compared against each other because skewness differs among regions and depth habitats; therefore, comparisons should be made only relative to variations within each individual record. **c**, EP cluster temperature skewness adjusted to the mean Niño 1+2 SST skewness and scaled using the temperature-skewness distribution derived from ERSST v5 for surface proxies (Fig. 1b) or ORA5 reanalysis for thermocline proxies (Fig. S3b), facilitating comparison across records. In all panels, dashed lines represent weighted linear regressions across multi-proxy types for the respective intervals while the linear trend is significant (dotted lines: insignificant, or too few samples to test). Errorbars show standard error due to sample size (Methods). Shaded vertical bars in the background denote the HS1, BA, and YD periods. Green texts in the legend denote surface/mixed layer or thermocline proxies.

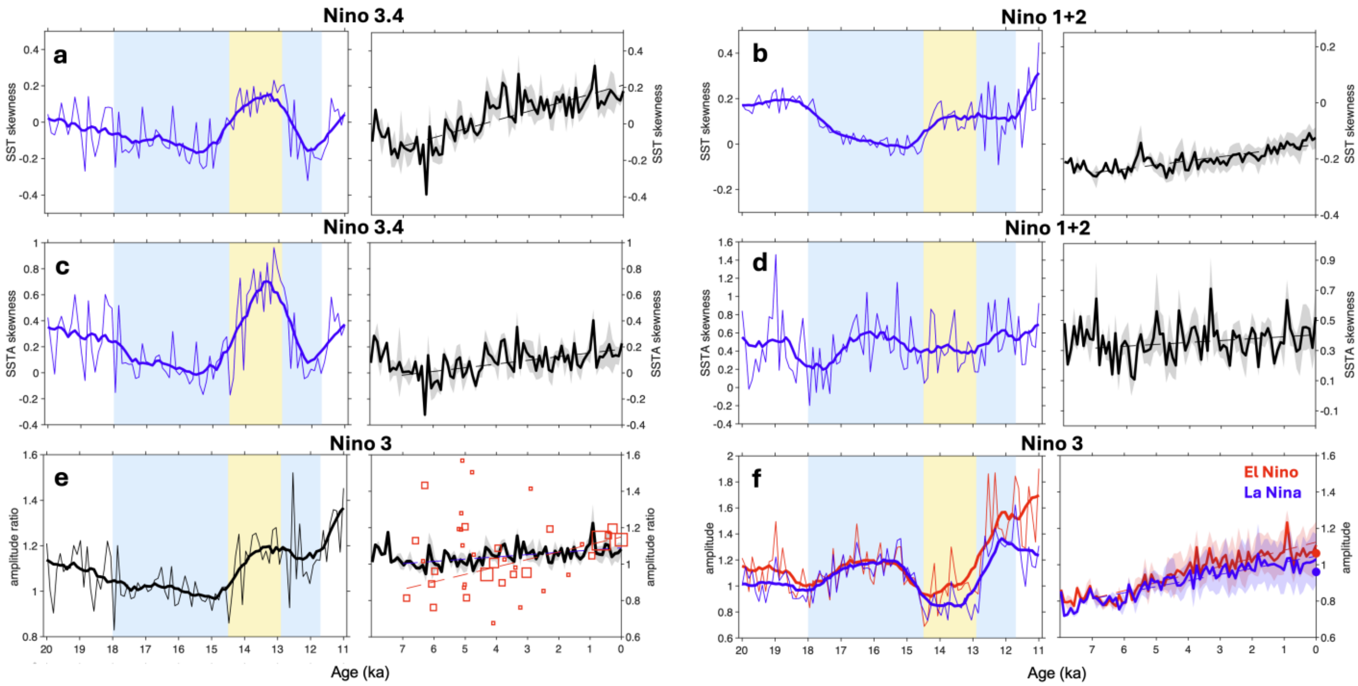

Figure 3 | Simulated ENSO asymmetry and amplitude since the LGM. a-d, Temporal evolution of skewness for (**a, c**) Niño 3.4 SST and SSTA and (**b, d**) Niño 1+2 SST and SSTA within transient climate simulations. Note the discontinuity between the Holocene (ensemble mean of 4 models, shading indicates ±0.5 standard deviation) and the deglacial period (iTRACE simulation only, sliding windows of 100-year, 5-point running mean). **e**, The ratio of El Niño-to-La Niña amplitude (Methods), denoting shifts in Niño 3 (5°S-5°N, 150-90°W) ENSO amplitude asymmetry. **f**, Evolution of El Niño (red) and La Niña (blue) amplitudes. In **e**, overlapping red squares represent individual CP fossil coral $\delta^{18}O$ (‰)-derived estimates, and in **f**, ERSST v5 reference values are shown as red & blue dots at 0 ka. The dashed lines in the Holocene ensembles indicate linear trends.

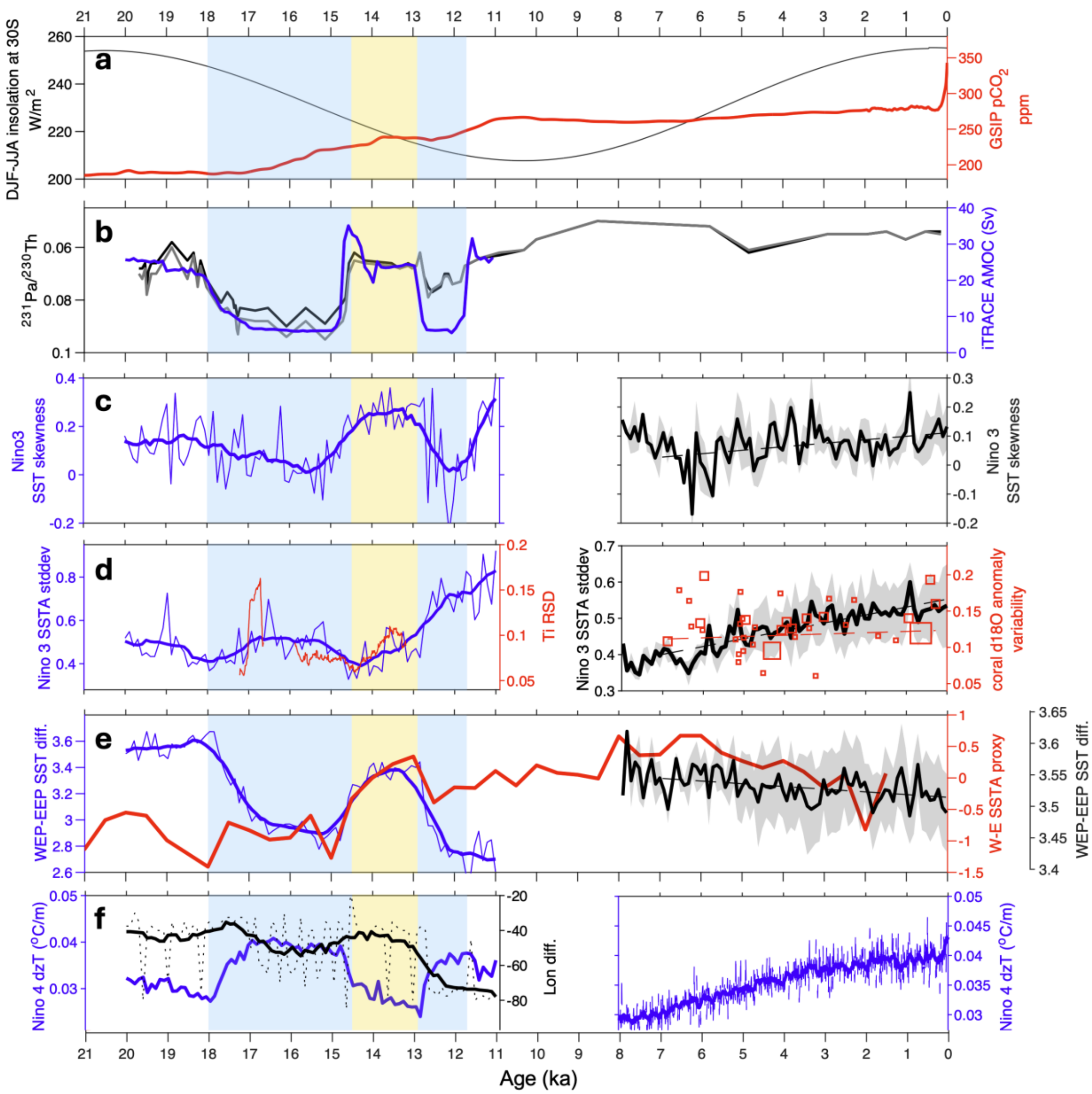

Figure 4 | Mechanistic drivers of evolving ENSO amplitude asymmetry. a, Evolution of Holocene seasonal orbital forcing at 60°N, JJA denoting precession signal (grey line) and melt water forcing in iTRACE (black). **b**, Comparison of simulated (blue) AMOC strength[89] with reconstructions (black)[90]. **c**, Simulated Nino 3 SST skewness during the deglaciation (iTRACE) and the Holocene (ensemble mean). **d**, Simulated ENSO variability represented by the standard deviation of simulated Niño 3 SSTA (blue and black lines, for iTRACE and the Holocene ensemble, respectively), and reconstruction from marine sediment records[63] (red line) and fossil corals (red squares). **e**, the reconstructed West-East SST difference (red)[56], and those simulated (5°S-5°N, 120-160°E - 5°S-5°N, 120-80°W) in iTRACE (blue line) and the Holocene simulations (black line). **f**, Simulated upper-ocean stratification (equivalent to thermocline depth) dzT for the tropical Eastern Pacific from iTRACE and EC-Earth (due to data availability) (blue lines), and the zonal distance (in longitude; also see Fig. S8) between the identified CP and EP El Niño centers of action in iTRACE (black line).

Acknowledgements

ZL acknowledges the Swedish Research Council Vetenskapsrådet (Grant no. 2022-03617), the Xiamen University Nanqiang Young Talents Program, and the Swedish Strategic Research Area MERGE (Modeling the Regional and Global Earth System). QZ is funded by the Swedish Research Council Vetenskapsrådet (Grant no. 2017-04232; 2022-03129). XS is supported by the Southern Marine Science and Engineering Guangdong Laboratory (Zhuhai) (grant no. SML2023SP204), the National Natural Science Foundation of China (NSFC) (grant no. 42206256) and the Ocean Negative Carbon Emissions (ONCE) Program. The EC-Earth simulations were performed on resources provided by the National Academic Infrastructure for Supercomputing in Sweden (NAISS) at Linköping University. The LOVECLIM1.3 simulations were performed with the support of the Fonds de la Recherche Scientifique-FNRS research grant no. T.0246.23. The IPSL simulation was performed as part of the GENCI computing project gen2212 and gen12006 on the TGCC computing center. They were supported by JPI-Belmont project PACMEDY (ANR-15-JCLI-0003-01). The HadCM3 simulations were run on the University of Birmingham's BlueBEAR HPC service (http://www.birmingham.ac.uk/bear) and supported through a Birmingham Fellowship to P.O.H. Computations for KCM were carried out on the NEC-SX Aurora TSUBASA at the computing centre of the Christian-Albrechts-University Kiel, Germany. We thank Dr. Aleksey Sadekov for sharing the original IFA data. ZL thanks Profs. Wenju Cai and Zhengyu Liu for insightful discussions.

Author contribution

Z.L. conceived this study. Z.L. analysed the data with input from M.C. Holocene transient simulations were performed by P.B., P.H., J.J., X.S., Q.Y. B.S, Y.H. and Q.Z. All authors interpreted and discussed the results. Z.L. wrote the paper with contributions from all authors. All authors reviewed the manuscript.

Competing interests

The authors declare no competing interests.

Data availability

The Nino 3.4, 3 and 1+2 SST time series (NetCDF files) from all 9 Holocene transient simulations are available from https://lu.box.com/s/p3ol7km03kqkbml6ll8zjn084zknwjar, and will be made available on Zenodo upon publication.

Mollusk data and metadata are compiled and archived in Figshare by Carré et al. (https://doi.org/10.6084/m9.figshare.14256434)

All fossil coral data and metadata are compiled and archived at NCDC by Grothe et al. (https://www.ncdc.noaa.gov/paleo/study/22415).

Marine sediment IFA data can be accessed at:

https://www.ncei.noaa.gov/access/paleo-search/study/23730
https://www.ncei.noaa.gov/access/paleo-search/study/26871
https://www.nature.com/articles/s41586-024-07984-y ("Source data")
https://www.ncei.noaa.gov/access/paleo-search/study/39479
https://paleo.ltrr.arizona.edu/contributions_by_author/koutavas2012/
https://doi.pangaea.de/10.1594/PANGAEA.841638
https://agupubs.onlinelibrary.wiley.com/doi/full/10.1029/2008PA001701 ("Supporting Information")

ERSST v5 reanalysis can be accessed at https://psl.noaa.gov/data/gridded/data.noaa.ersst.v5.html

ORA5 reanalysis can be accessed at https://cds.climate.copernicus.eu/datasets/reanalysis-oras5

TRACE simulation can be accessed at https://gdex.ucar.edu/datasets/d651050/
iTRACE simulation can be accessed at https://gdex.ucar.edu/datasets/d651022/

Code availability

The Matlab code to produce the main figures of this manuscript will be made available on Zenodo upon publication.

References

1 McPhaden, M. J., Santoso, A. & Cai, W. Introduction to El Niño Southern Oscillation in a changing climate. *El Niño Southern Oscillation in a changing climate*, 1–19 (2020).

2 Timmermann, A. *et al.* El Niño–southern oscillation complexity. *Nature* **559**, 535–545 (2018).

3 An, S. I., Tziperman, E., Okumura, Y. M. & Li, T. ENSO irregularity and asymmetry. *El Niño Southern Oscillation in a changing climate*, 153–172 (2020).

4 Santoso, A., McPhaden, M. J. & Cai, W. The defining characteristics of ENSO extremes and the strong 2015/2016 El Niño. *Reviews of Geophysics* **55**, 1079–1129 (2017).

5 Callahan, C. W. & Mankin, J. S. Persistent effect of El Niño on global economic growth. *Science* **380**, 1064–1069 (2023).

6 Liu, Y., Cai, W., Lin, X., Li, Z. & Zhang, Y. Nonlinear El Niño impacts on the global economy under climate change. *Nature Communications* **14**, 5887 (2023).

7 Liu, J. *et al.* Contrasting carbon cycle responses of the tropical continents to the 2015–2016 El Niño. *Science* **358**, eaam5690 (2017).

8 Okumura, Y. M. & Deser, C. Asymmetry in the duration of El Niño and La Niña. *Journal of Climate* **23**, 5826–5843 (2010).

9 Geng, T. *et al.* Increased occurrences of consecutive La Niña events under global warming. *Nature* **619**, 774–781 (2023). https://doi.org/10.1038/s41586-023-06236-9

10 Okumura, Y. M., DiNezio, P. & Deser, C. Evolving Impacts of Multiyear La Niña Events on Atmospheric Circulation and U.S. Drought. *Geophysical Research Letters* **44**, 11,614–611,623 (2017). https://doi.org/https://doi.org/10.1002/2017GL075034

11 Cai, W. *et al.* Increased variability of eastern Pacific El Niño under greenhouse warming. *Nature* **564**, 201–206 (2018).

12 Planton, Y. Y. *et al.* Evaluating climate models with the CLIVAR 2020 ENSO metrics package. *Bulletin of the American Meteorological Society* **102**, E193–E217 (2021).

13 An, S. I. Interdecadal changes in the El Nino–La Nina asymmetry. *Geophysical Research Letters* **31** (2004).

14 Geng, T., Cai, W. & Wu, L. Two types of ENSO varying in tandem facilitated by nonlinear atmospheric convection. *Geophysical Research Letters* **47**, e2020GL088784 (2020).

15 Cai, W. *et al.* Changing El Niño–Southern Oscillation in a warming climate. *Nature Reviews Earth & Environment* **2** (2021). https://doi.org/10.1038/s43017-021-00199-z

16 Geng, T., Cai, W., Jia, F. & Wu, L. Decreased ENSO post-2100 in response to formation of a permanent El Niño-like state under greenhouse warming. *Nature communications* **15**, 5810 (2024).

17 Geng, T. & Cai, W. Enhanced eastern Pacific warming weakens ENSO asymmetry post-2100 under persistent greenhouse warming. *Geophysical Research Letters* **52**, e2025GL115407 (2025).

18 Peng, Q., Xie, S.-P. & Deser, C. Collapsed upwelling projected to weaken ENSO under sustained warming beyond the twenty-first century. *Nature Climate Change* **14**, 815–822 (2024).

19 Liang, J. *et al.* The Asymmetry of the El Niño–Southern Oscillation: Characteristics, Mechanisms, and Implications for a Changing Climate. *Atmosphere* **16**, 1071 (2025).

20 Geng, T., Cai, W., Wu, L. & Yang, Y. Atmospheric convection dominates genesis of ENSO asymmetry. *Geophysical Research Letters* **46**, 8387–8396 (2019).

21 Choi, K.-Y., Vecchi, G. A. & Wittenberg, A. T. ENSO transition, duration, and amplitude asymmetries: Role of the nonlinear wind stress coupling in a conceptual model. *Journal of Climate* **26**, 9462–9476 (2013).

22 Frauen, C. & Dommenget, D. El Niño and La Niña amplitude asymmetry caused by atmospheric feedbacks. *Geophysical Research Letters* **37** (2010).

23 Kang, I. S. & Kug, J. S. El Niño and La Niña sea surface temperature anomalies: Asymmetry characteristics associated with their wind stress anomalies. *Journal of Geophysical Research: Atmospheres* **107**, ACL–1 (2002).

24 Jin, F. F., Lin, L., Timmermann, A. & Zhao, J. Ensemble-mean dynamics of the ENSO recharge oscillator under state-dependent stochastic forcing. *Geophysical research letters* **34** (2007).

25 Levine, A., Jin, F. F. & McPhaden, M. J. Extreme noise–extreme El Niño: How state-dependent noise forcing creates El Niño–La Niña asymmetry. *Journal of Climate* **29**, 5483–5499 (2016).

26 Yu, S. & Fedorov, A. V. The essential role of westerly wind bursts in ENSO dynamics and extreme events quantified in model “wind stress shaving” experiments. *Journal of Climate* **35**, 7519–7538 (2022).

27 Jin, F. F., An, S. I., Timmermann, A. & Zhao, J. Strong El Niño events and nonlinear dynamical heating. *Geophysical research letters* **30**, 20–21 (2003).

28 Su, J. *et al.* Causes of the El Niño and La Niña amplitude asymmetry in the equatorial eastern Pacific. *Journal of Climate* **23**, 605–617 (2010).

29 An, S.-I. Interannual variations of the tropical ocean instability wave and ENSO. *Journal of Climate* **21**, 3680–3686 (2008).

30 An, S. I. & Kim, J. W. Role of nonlinear ocean dynamic response to wind on the asymmetrical transition of El Niño and La Niña. *Geophysical Research Letters* **44**, 393–400 (2017).

31 Im, S. H., An, S. I., Kim, S. T. & Jin, F. F. Feedback processes responsible for El Niño-La Niña amplitude asymmetry. *Geophysical Research Letters* **42**, 5556–5563 (2015).

32 Kim, S. K. & An, S. I. Untangling El Niño-La Niña asymmetries using a nonlinear coupled dynamic index. *Geophysical Research Letters* **47**, e2019GL085881 (2020).

33 An, S.-I. & Jin, F.-F. Nonlinearity and asymmetry of ENSO. *Journal of Climate* **17**, 2399–2412 (2004).

34 Hayashi, M. & Watanabe, M. ENSO complexity induced by state dependence of westerly wind events. *Journal of Climate* **30**, 3401–3420 (2017).

35 Shakun, J. D. *et al.* Global warming preceded by increasing carbon dioxide concentrations during the last deglaciation. *Nature* **484**, 49–54 (2012).

36 Cobb, K. M. *et al.* Highly variable El Niño–southern oscillation throughout the Holocene. *Science* **339**, 67–70 (2013).

37 Carré, M. *et al.* Holocene history of ENSO variance and asymmetry in the eastern tropical Pacific. *Science* **345**, 1045–1048 (2014).

38 Emile-Geay, J. *et al.* Links between tropical Pacific seasonal, interannual and orbital variability during the Holocene. *Nature Geoscience* **9**, 168–173 (2016).

39 Moy, C. M., Seltzer, G. O., Rodbell, D. T. & Anderson, D. M. Variability of El Niño/Southern Oscillation activity at millennial timescales during the Holocene epoch. *Nature* **420**, 162–165 (2002).

40 Ford, H. L., Ravelo, A. C. & Polissar, P. J. Reduced El Niño–Southern Oscillation during the last glacial maximum. *Science* **347**, 255–258 (2015).

41 Li, J. *et al.* El Niño modulations over the past seven centuries. *Nature climate change* **3**, 822–826 (2013).

42 Thirumalai, K. *et al.* Future increase in extreme El Niño supported by past glacial changes. *Nature* **634**, 374–380 (2024).

43 Lu, Z., Liu, Z., Zhu, J. & Cobb, K. M. A Review of Paleo El Niño-Southern Oscillation. *Atmosphere* **9**, 130 (2018).

44 Iwakiri, T. & Watanabe, M. MECHANISMs Reducing ENSO amplitude and asymmetry via an enhanced seasonal cycle in the mid-Holocene. *Journal of Climate* **32**, 8069–8085 (2019).

45 Clark, P. U. *et al.* The last glacial maximum. *science* **325**, 710–714 (2009).

46 Huang, B. *et al.* Extended reconstructed sea surface temperature, version 5 (ERSSTv5): upgrades, validations, and intercomparisons. *Journal of Climate* **30**, 8179–8205 (2017).

47 Copernicus Climate Change Service, C. D. S. ORAS5 global ocean reanalysis monthly data from 1958 to present. *Copernicus Climate Change Service (C3S) Climate Data Store (CDS)* (2021).

48 Burgers, G. & Stephenson, D. B. The "normality" of el niño. *Geophysical Research Letters* **26**, 1027–1030 (1999).

49 Li, T. & Philander, S. G. H. On the annual cycle of the eastern equatorial Pacific. *Journal of Climate*, 2986–2998 (1996).

50 Khon, V. C., Schneider, B., Latif, M., Park, W. & Wengel, C. Evolution of eastern equatorial Pacific seasonal and interannual variability in response to orbital forcing during the Holocene and Eemian from model simulations. *Geophysical Research Letters* **45**, 9843–9851 (2018).

51 Kim, H., Kang, S. M., Kay, J. E. & Xie, S.-P. Subtropical clouds key to Southern Ocean teleconnections to the tropical Pacific. *Proceedings of the National Academy of Sciences* **119**, e2200514119 (2022).

52 Xie, S.-P. *et al.* A regional ocean–atmosphere model for eastern Pacific climate: toward reducing tropical biases. *Journal of Climate* **20**, 1504–1522 (2007).

53 Karamperidou, C. & DiNezio, P. N. Holocene hydroclimatic variability in the tropical Pacific explained by changing ENSO diversity. *Nature Communications* **13**, 7244 (2022).

54 He, C. *et al.* Hydroclimate footprint of pan-Asian monsoon water isotope during the last deglaciation. *Science Advances* **7**, eabe2611 (2021).

55 Liu, Z. *et al.* Evolution and forcing mechanisms of El Niño over the past 21,000 years. *Nature* **515**, 550 (2014).

56 Koutavas, A. & Joanides, S. El Niño–Southern oscillation extrema in the holocene and last glacial maximum. *Paleoceanography* **27** (2012).

57 Lu, Z. *et al.* Increased frequency of multi-year El Niño–Southern Oscillation events across the Holocene. *Nature Geoscience* **18**, 337–343 (2025).

58 Koutavas, A., Lynch-Stieglitz, J., Marchitto Jr, T. M. & Sachs, J. P. El Nino-like pattern in ice age tropical Pacific sea surface temperature. *Science* **297**, 226–230 (2002).

59 Carré, M. *et al.* Mid-Holocene mean climate in the south eastern Pacific and its influence on South America. *Quaternary International* **253**, 55–66 (2012).

60 Xu, J., Kuhnt, W., Holbourn, A., Regenberg, M. & Andersen, N. Indo-Pacific warm pool variability during the Holocene and Last Glacial Maximum. *Paleoceanography* **25** (2010).

61 Timmermann, A. *et al.* The influence of a weakening of the Atlantic meridional overturning circulation on ENSO. *Journal of climate* **20**, 4899–4919 (2007).

62 Orihuela-Pinto, B., Santoso, A., England, M. H. & Taschetto, A. S. Reduced ENSO variability due to a collapsed Atlantic Meridional Overturning Circulation. *Journal of Climate* **35**, 5307–5320 (2022).

63 Yseki, M. *et al.* El Niño–Southern Oscillation strengthened by North Atlantic Iceberg discharge during Heinrich stadial 1. *Communications Earth & Environment* (2026).

64 Okumura, Y. M. ENSO diversity from an atmospheric perspective. *Current Climate Change Reports* **5**, 245–257 (2019).

65 Lu, Z., Liu, Z. & Zhu, J. Abrupt intensification of ENSO forced by deglacial ice-sheet retreat in CCSM3. *Climate dynamics* **46**, 1877–1891 (2016).

66 Luan, Y., Braconnot, P., Yu, Y. & Zheng, W. Tropical Pacific mean state and ENSO changes: sensitivity to freshwater flux and remnant ice sheets at 9.5 ka BP. *Climate dynamics* **44**, 661–678 (2015).

67 Lu, Z., Liu, Z., Chen, G. & Guan, J. Prominent Precession Band Variance in ENSO Intensity Over the Last 300,000 Years. *Geophysical Research Letters* **46**, 9786–9795 (2019).

68 Pontes, G. M. *et al.* Mid-pliocene el niño/southern oscillation suppressed by pacific intertropical convergence zone shift. *Nature Geoscience* **15**, 726–734 (2022).

69 Rafter, P. A. *et al.* Persistent eastern equatorial Pacific Ocean upwelling since the warm Pliocene. *Science* **390**, eads8720 (2025).

70 Braconnot, P. *et al.* Evaluation of climate models using palaeoclimatic data. *Nature Climate Change* **2**, 417–424 (2012).

71 Carré, M. *et al.* High-resolution marine data and transient simulations support orbital forcing of ENSO amplitude since the mid-Holocene. *Quaternary Science Reviews* **268**, 107125 (2021).

72 Lawman, A. E. *et al.* Unraveling forced responses of extreme El Niño variability over the Holocene. *Science Advances* **8**, eabm4313 (2022).

73 Grothe, P. R. *et al.* Enhanced El Niño–Southern oscillation variability in recent decades. *Geophysical Research Letters* **47**, e2019GL083906 (2020).

74 Grossman, E. L. & Ku, T.-L. Oxygen and carbon isotope fractionation in biogenic aragonite: temperature effects. *Chemical Geology: Isotope Geoscience Section* **59**, 59–74 (1986).

75 White, S. M., Ravelo, A. C. & Polissar, P. J. Dampened El Niño in the early and mid-Holocene due to insolation-forced warming/deepening of the thermocline. *Geophysical Research Letters* **45**, 316–326 (2018).

76 Leduc, G., Vidal, L., Cartapanis, O. & Bard, E. Modes of eastern equatorial Pacific thermocline variability: Implications for ENSO dynamics over the last glacial period. *Paleoceanography* **24** (2009).

77 Glaubke, R. H. *et al.* An inconsistent ENSO response to Northern Hemisphere stadials over the last deglaciation. *Geophysical Research Letters* **51**, e2023GL107634 (2024).

78 Anand, P., Elderfield, H. & Conte, M. H. Calibration of Mg/Ca thermometry in planktonic foraminifera from a sediment trap time series. *Paleoceanography* **18** (2003).

79 Berger, A. Long-term variations of daily insolation and Quaternary climatic changes. *Journal of Atmospheric Sciences* **35**, 2362–2367 (1978).

80 Otto-Bliesner, B. L. *et al.* The PMIP4 contribution to CMIP6–Part 2: Two interglacials, scientific objective and experimental design for Holocene and Last Interglacial simulations. *Geoscientific Model Development* **10**, 3979–4003 (2017).

81 Tierney, J. E. *et al.* Glacial cooling and climate sensitivity revisited. *Nature* **584**, 569–573 (2020).

82 Zhang, Q. *et al.* Simulating the mid-Holocene, last interglacial and mid-Pliocene climate with EC-Earth3-LR. *Geoscientific Model Development* **14**, 1147–1169 (2021).

83 Braconnot, P. *et al.* Impact of multiscale variability on last 6,000 years Indian and West African monsoon rain. *Geophysical Research Letters* **46**, 14021–14029 (2019).

84 Dallmeyer, A. *et al.* Holocene vegetation transitions and their climatic drivers in MPI-ESM1. 2. *Climate of the Past* **17**, 2481–2513 (2021).

85 Shi, X. *et al.* Calendar effects on surface air temperature and precipitation based on model-ensemble equilibrium and transient simulations from PMIP4 and PACMEDY. *Climate of the Past* **18**, 1047–1070 (2022).

86 Deuser, W. G., Ross, E. H., Hemleben, C. & Spindler, M. Seasonal changes in species composition, numbers, mass, size, and isotopic composition of planktonic foraminifera settling into the deep Sargasso Sea. *Palaeogeography, Palaeoclimatology, Palaeoecology* **33**, 103–127 (1981).

87 Davis, C. V., Fuqua, L., Pride, C. & Thunell, R. Seasonal and interannual changes in planktic foraminiferal fluxes and species composition in Guaymas Basin, Gulf of California. *Marine Micropaleontology* **149**, 75–88 (2019).

88 Takahashi, K., Montecinos, A., Goubanova, K. & Dewitte, B. ENSO regimes: Reinterpreting the canonical and Modoki El Niño. *Geophysical research letters* **38** (2011).

89 Zhu, C. *et al.* Enhanced ocean heat storage efficiency during the last deglaciation. *Science Advances* **10**, eadp5156 (2024).

90 McManus, J. F., Francois, R., Gherardi, J. M., Keigwin, L. D. & Brown-Leger, S. Collapse and rapid resumption of Atlantic meridional circulation linked to deglacial climate changes. *nature* **428**, 834–837 (2004).

This PDF file includes:

Supplementary Figure 1 to 13
Supplementary Table 1 to 2

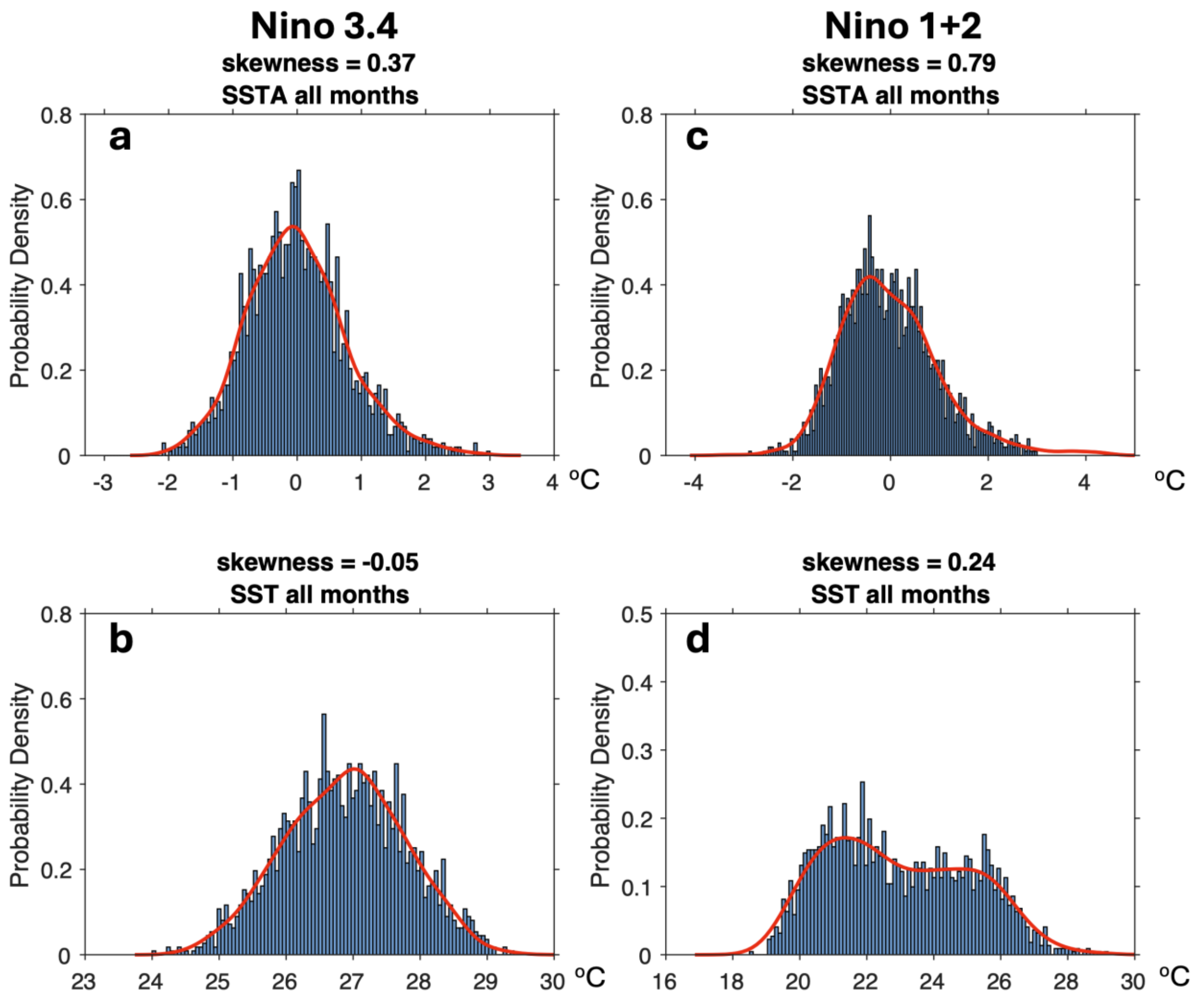

Supplementary Figure 1 | Probability density functions of ERSST v5. a, b, Probability density functions (PDFs) of Niño 3.4 region sea surface temperature anomalies (SSTA, **a**) and SST (**b**) derived from the ERSST v5 dataset (1854–2025). **c, d**, Corresponding PDFs for the Niño 1+2 region (SSTA, **c**; SST, **d**). In all panels, the solid red line indicates the non-parametric Kernel Density Estimate (KDE) used to calculate the skewness, providing a continuous fit to the discrete reanalysis data.

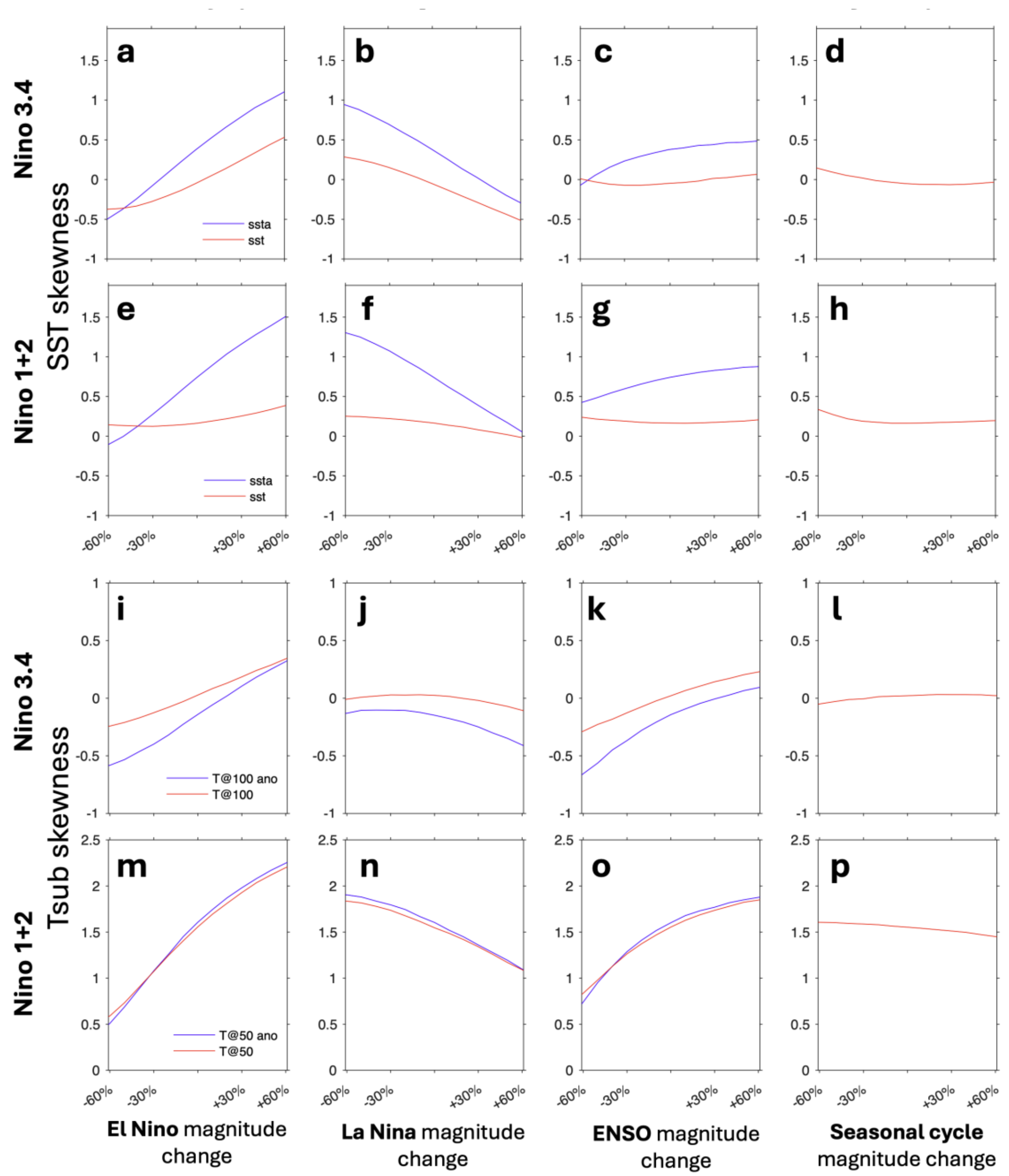

Supplementary Figure 2 | Sensitivity of skewness to isolated ENSO and seasonal cycle amplitude perturbations. a–h, Response of SSTA skewness (blue) and SST skewness (red) to idealised amplitude perturbations. **a–c, e–g**, Effects of systematically increasing or decreasing the amplitude (±10% to ±60%) of isolated El Niño events (**a, e**), isolated La Niña events (**b, f**), and both phases simultaneously (**c, g**). **d, h**, Impact of scaling the amplitude of the climatological seasonal cycle (±10% to ±60%) on the total SST skewness while maintaining constant anomaly variance. ENSO events are identified by Niño 3 SSTA (Methods). **i–p**, same as **a–h**, but for thermocline temperature (red) and thermocline temperature anomalies (blue). The depth at which the thermocline temperature is used is ~100m in Niño 3.4 and ~50m in Niño 1+2.

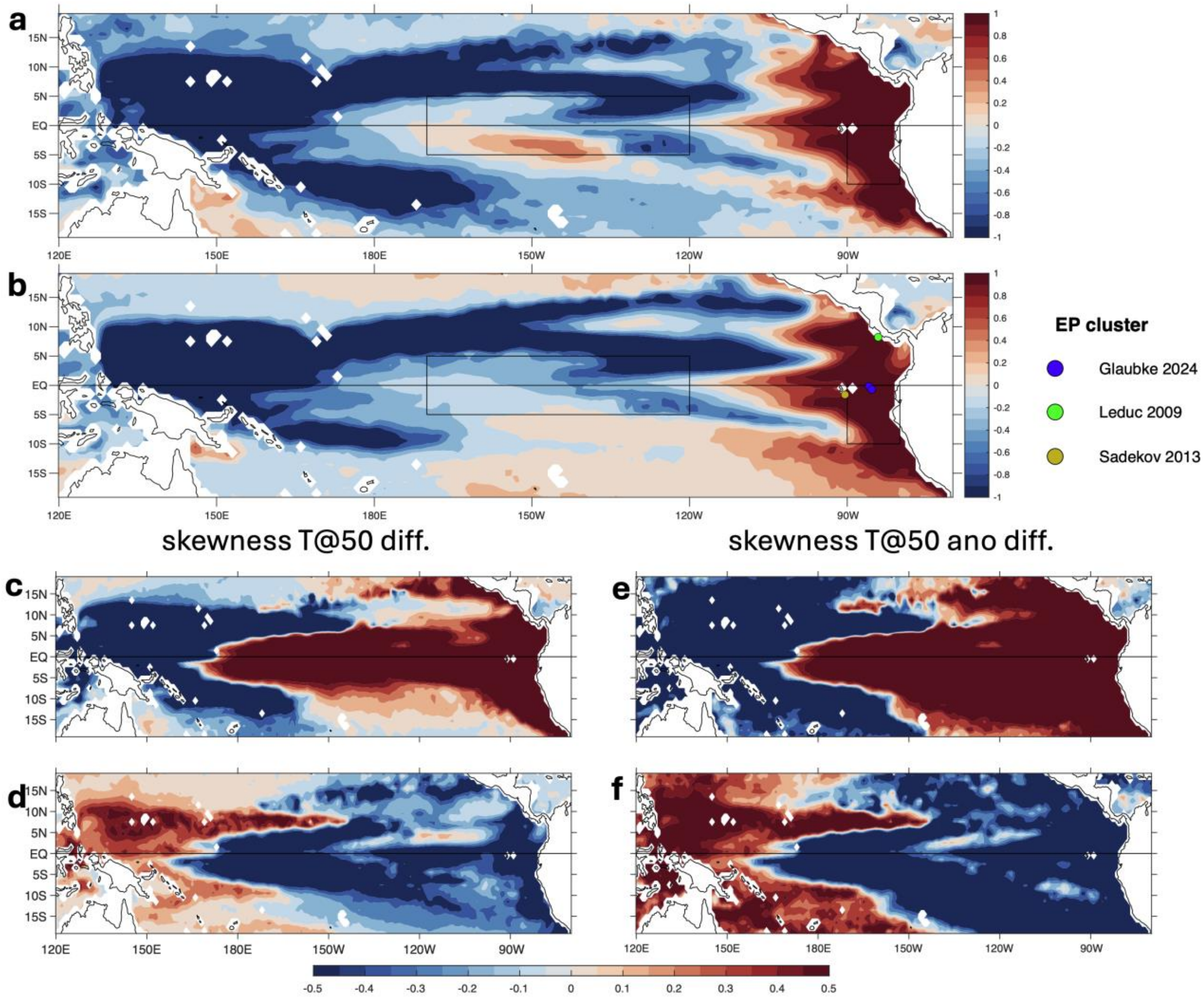

Supplementary Figure 3 | Spatial patterns and sensitivity of tropical Pacific thermocline aea temperature skewness at~50m depth. Same as **Fig. 1**, but using subsurface sea temperature at ~50m depth from ORA5 reanalysis data of 1958-2025.

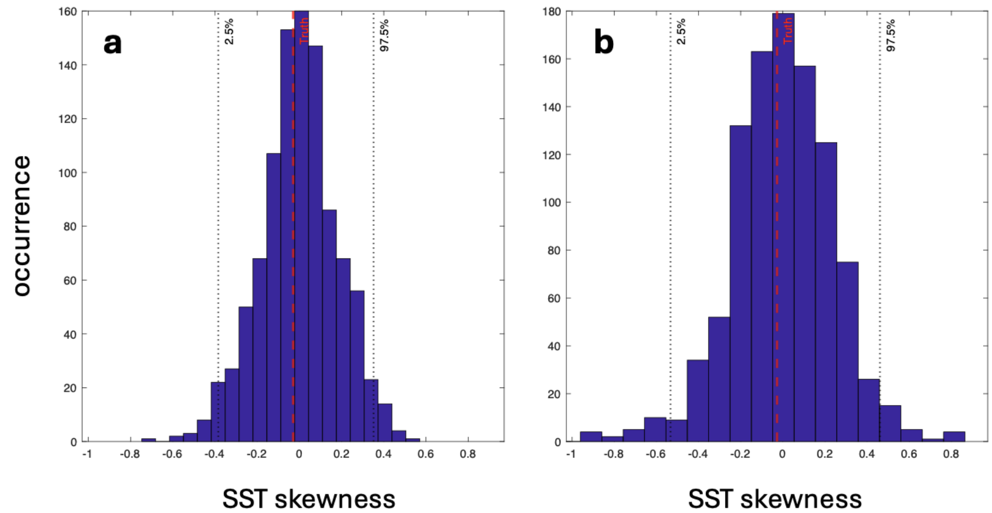

Supplementary Figure 4 | Uncertainty quantification of skewness estimates relative to sample size. Estimates of sampling uncertainty for Niño 3.4 SST skewness. The "truth" (red vertical dashed line) is defined by the full 2,064-month ERSST v5 reanalysis (1854–2025). Blue bars represent the PDF of skewness values derived from 10,000 iterations of random subsampling (n = (a) 60 and (b) 120 months per iteration), and its standard deviation is used for uncertainty estimate in **Fig. 2**. The spread of the distribution illustrates the statistical noise inherent in short-duration discrete proxy records.

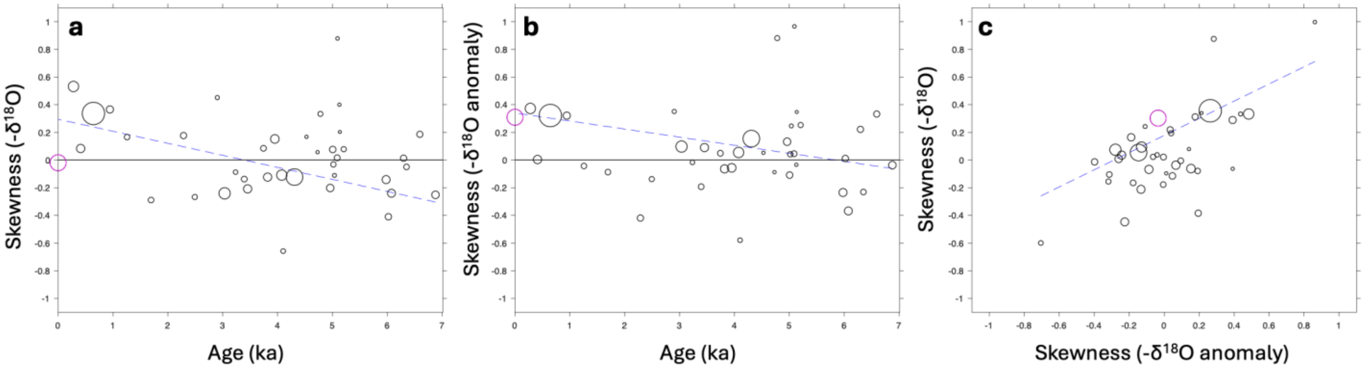

Supplementary Figure 5 | Evolution of Central Pacific fossil coral $\delta^{18}O$ (‰) and $\delta^{18}O$ anomaly skewness and their relationship. a, Time series of Central Pacific (CP) fossil coral $\delta^{18}O$ (‰) skewness (sign-inverted for consistency with SST) over the last 7 ka, also shown as red squares in Fig. 2a, and **b**, same as **a** but for $\delta^{18}O$ (‰) anomaly (corresponding to SSTA) skewness. **c**, Linear regression showing the relationship between coral $\delta^{18}O$ (‰) skewness and coral $\delta^{18}O$ (‰) anomaly skewness across the Holocene.

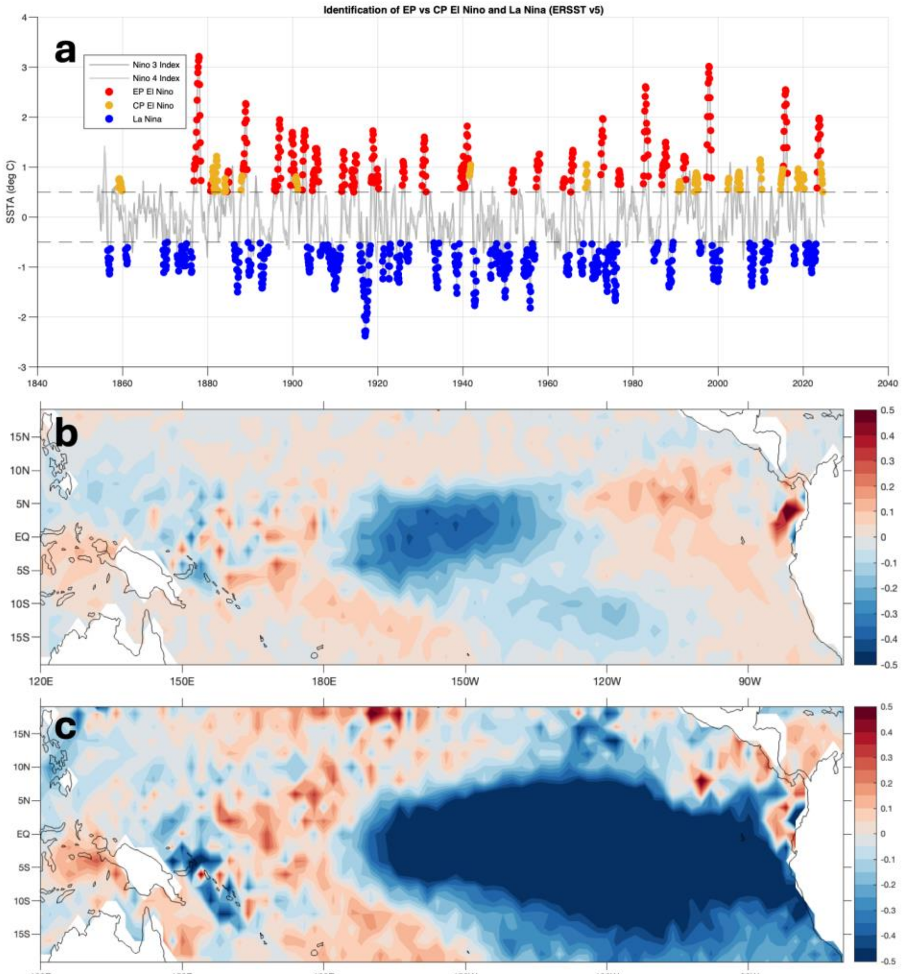

Supplementary Figure 6 | Influence of ENSO flavor on basin-wide skewness distribution. a, Identification of Eastern Pacific (EP) El Niño, Central Pacific (CP) El Niño, and La Niña events in the ERSST v5 reanalysis based on the Takahashi et al. (2011) E and C indices (Methods). **b, c**, Spatial maps showing the change in (**b**) absolute SST skewness and (**c**) SSTA skewness when EP El Niño months and CP El Niño months are selectively excluded (no “EP El Niño” – no “CP El Niño” conditions), isolating the relative contribution of each "flavor" to the spatial pattern of skewness.

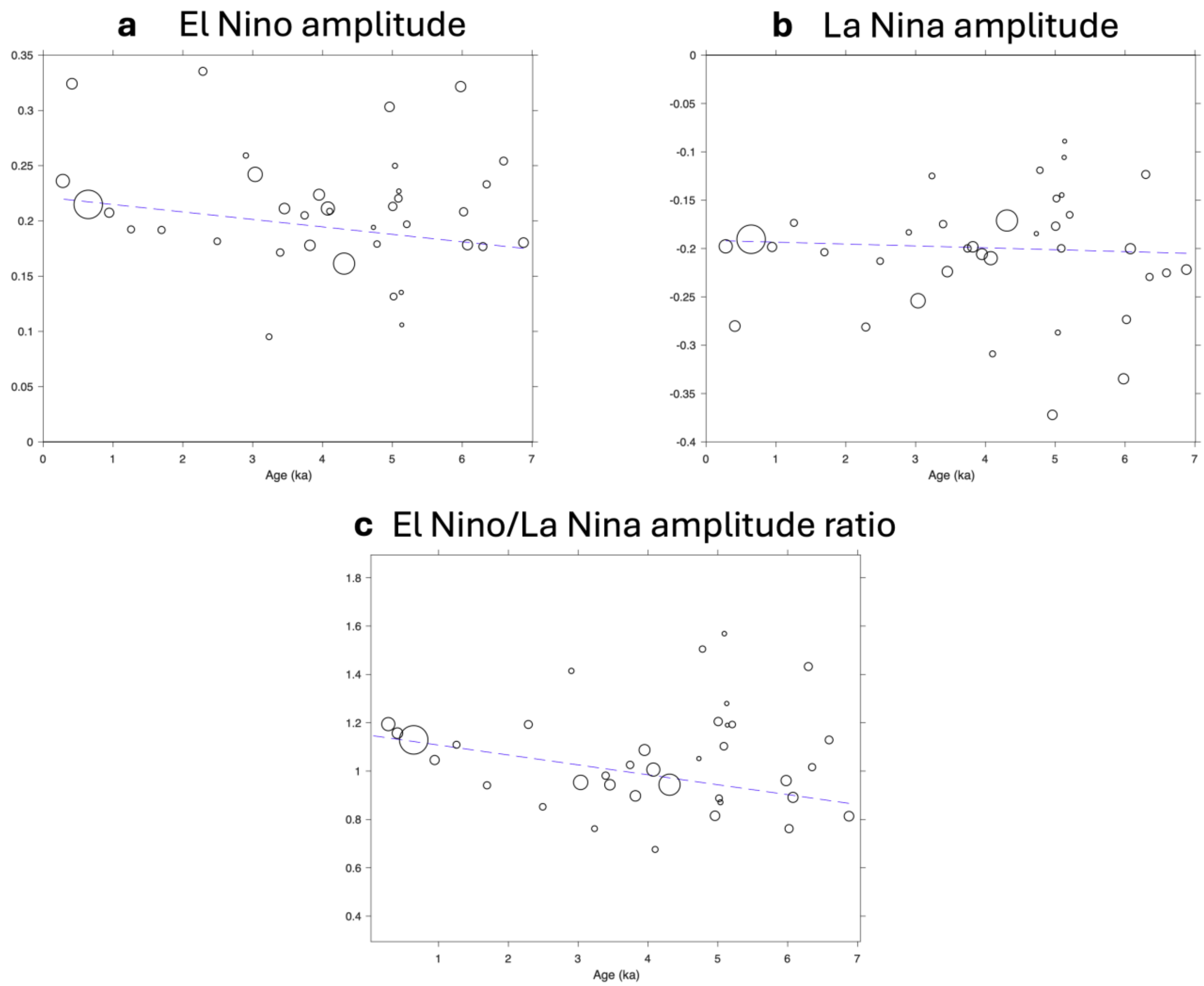

Supplementary Figure 7 | ENSO asymmetry and amplitude evolution during the Holocene from fossil coral data. a, **b,** individual CP fossil coral δ18O (‰)-derived estimates for El Niño and La Niña amplitudes. And **c**, their amplitude ratio, same as **Fig. 3e** red squares.

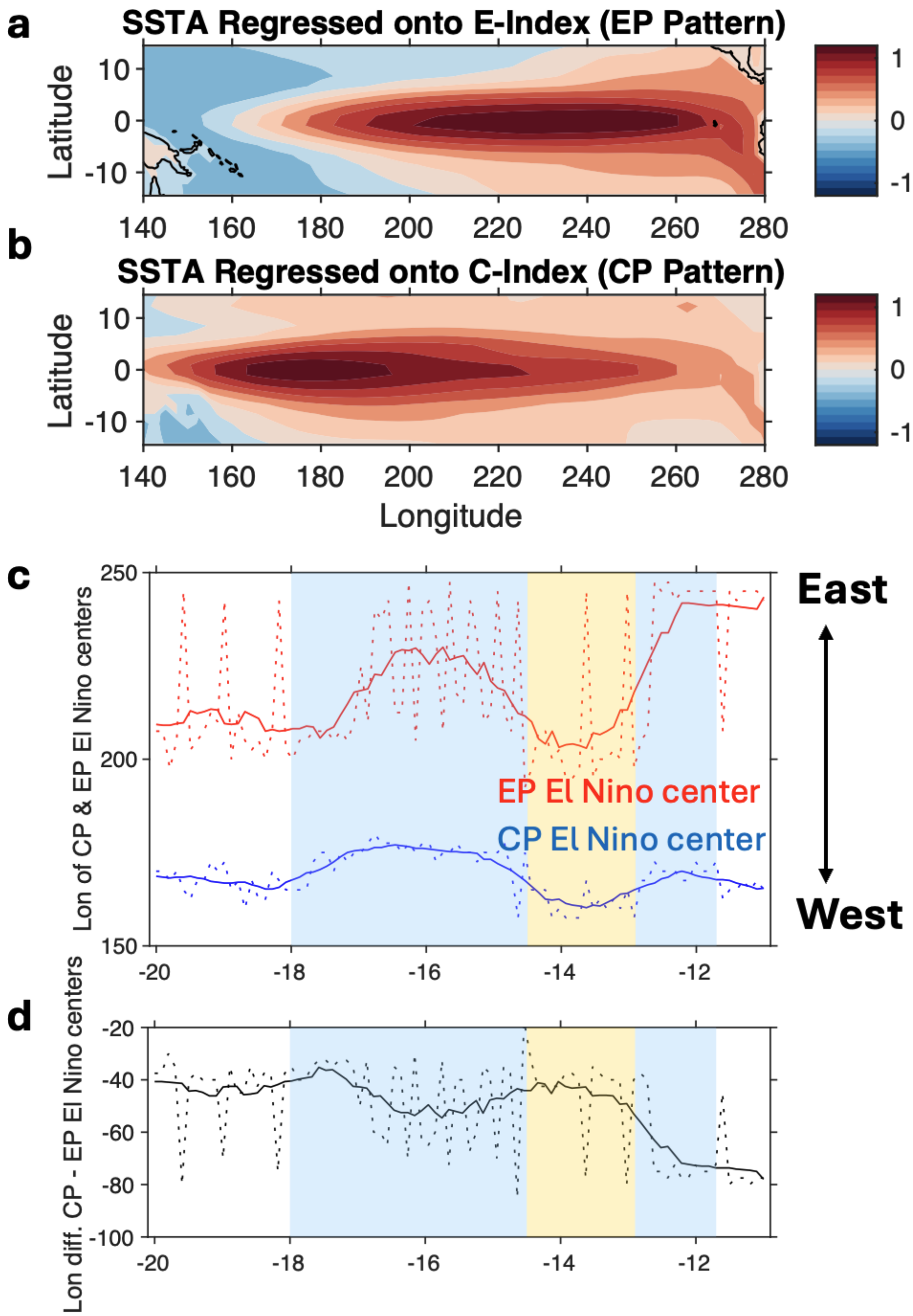

Supplementary Figure 8 | Spatial characteristics of ENSO flavors in transient iTRACE simulation. a,b, Spatial patterns of EP and CP El Niño events within the iTRACE transient simulation (in the last 200 model years), identified via regression of SSTA onto the rotated E and C indices (Methods). **c**, The longitudinal migration of the center of action (peak warming location) for both CP and EP flavors (in blue and red colors) throughout the deglacial period, and **d**, their distance in longitude.

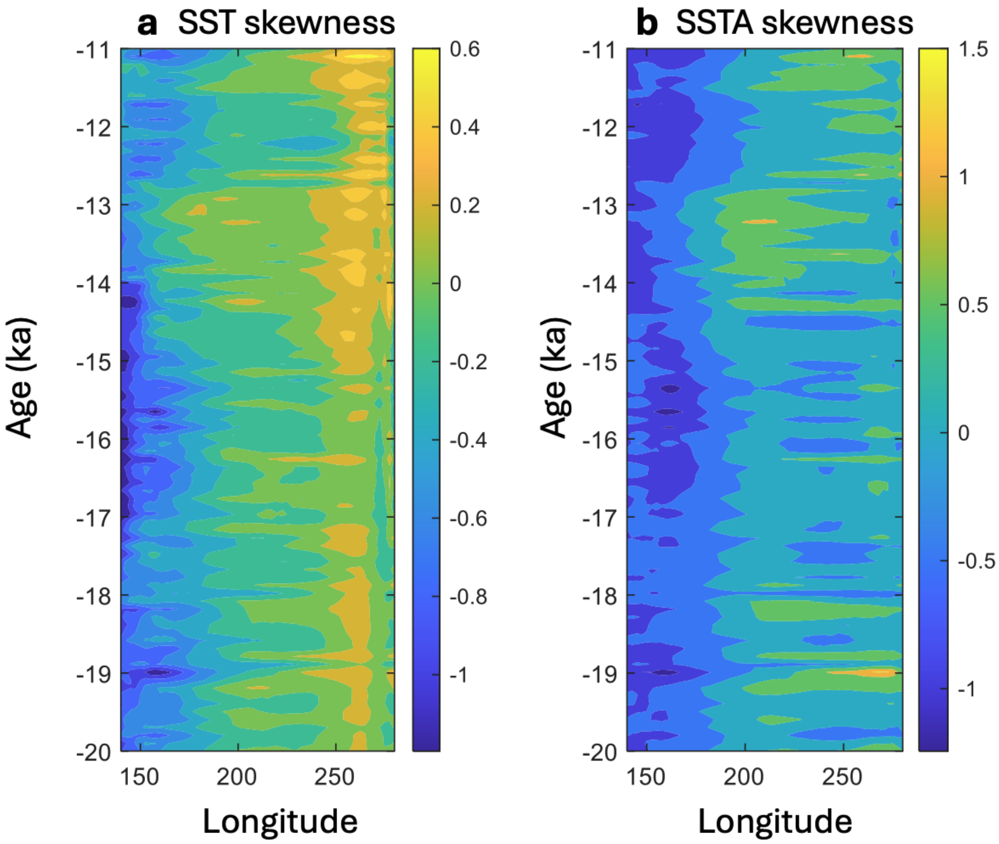

Supplementary Figure 9 | Evolution of SST and SSTA skewness along the equator in iTRACE. Hovmoller diagrams of SST and SSTA skewness in iTRACE (between 5°S and 5°N).

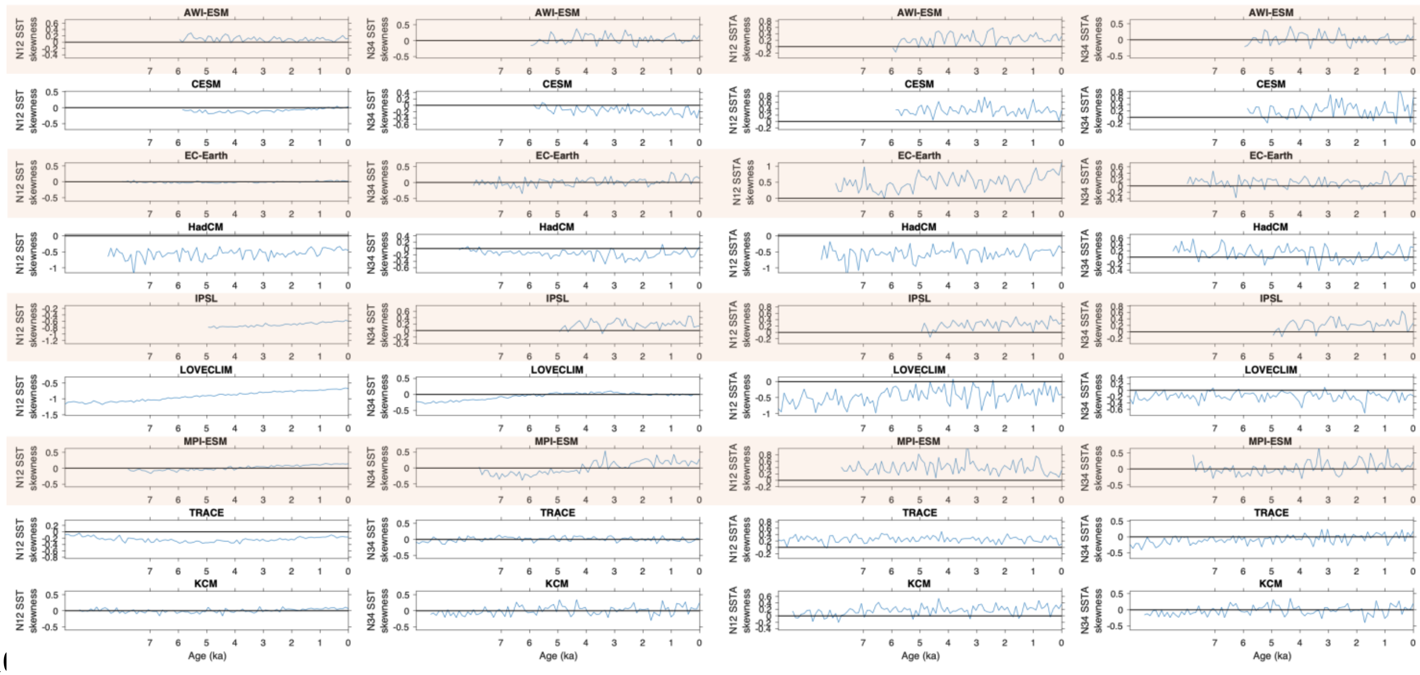

Supplementary Figure 10 | Comparison of ENSO asymmetry (in SST and SSTA skewness) across Holocene transient simulations. Inter-model comparison of Niño 1+2 and Niño 3.4 SST and SSTA skewness across all 9 available Holocene transient simulations. From left to right: Niño 1+2 SST skewness, Niño 3.4 SST skewness, Niño 1+2 SSTA skewness, and Niño 3.4 SSTA skewness. Orange highlights indicate the four model runs selected for the main ensemble (**Fig. 3**) based on their performance on simulated SSTA skewness spatial patterns (see **Supplementary Figure 11**).

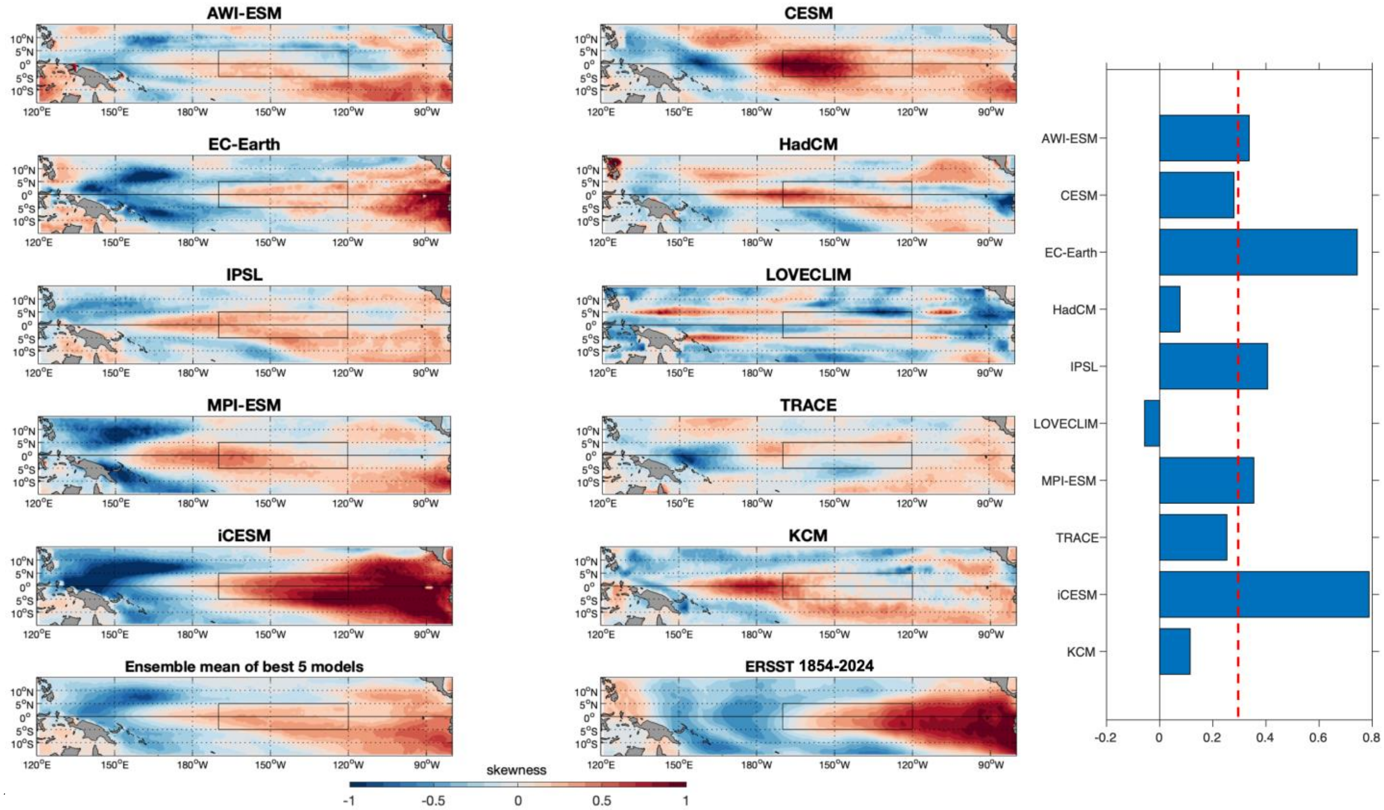

Supplementary Figure 11 | Evaluation of simulated vs. observed SSTA skewness spatial structure for model selection. (Left and mid columns**)** Spatial patterns of SSTA skewness over the last 100 years across all Holocene transient simulations compared to the ERSST v5 reanalysis (1854–2024), and all individual model patterns as well as the ensemble mean derived from the four best-performing models (Holocene: AWI-ESM, EC-Earth, IPSL, MPI-ESM; deglacial: iTRACE/iCESM). (Right column) Bars represent the spatial correlation coefficients between each model and the reanalysis, validating the ensemble's ability to represent the modern tropical Pacific variance asymmetry structure, and a threshold of 0.3 is chosen to select 4 out of 9 Holocene simulations.

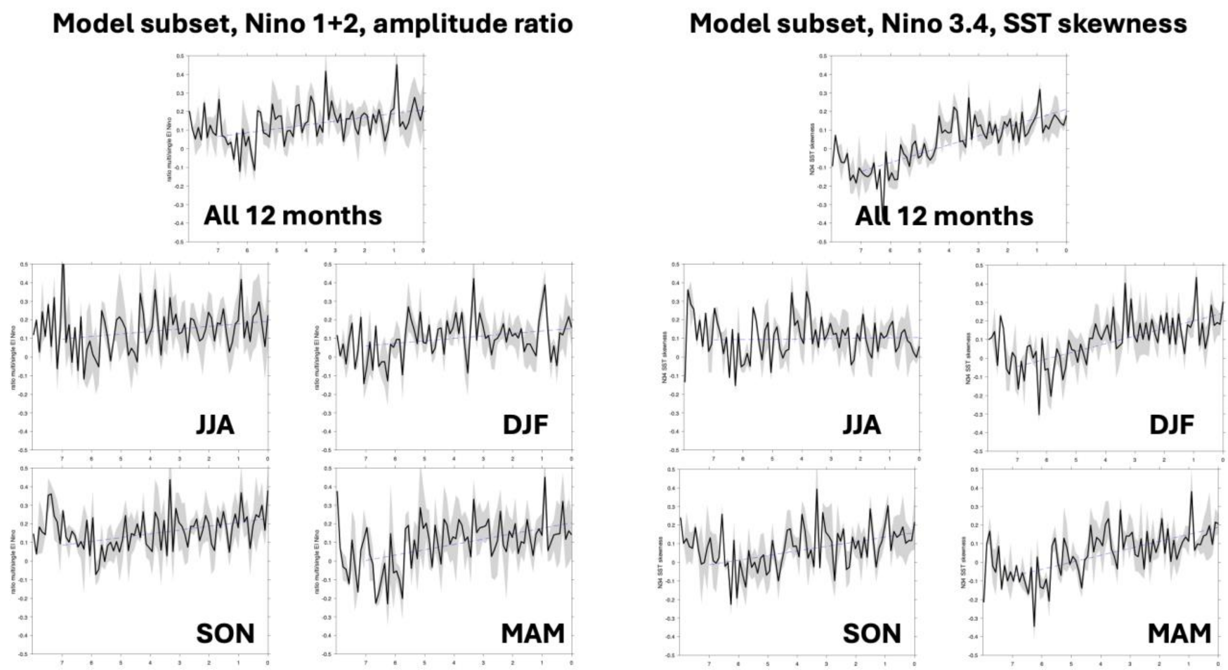

Supplementary Figure 12 | Uncertainty quantification of skewness estimates relative to foraminifera seasonal concentration. Comparison of Niño 1+2 ENSO amplitude ratio and Niño 3.4 SST skewness using all 12 months, and only 1 specific season (JJA, DJF, SON, MAM) in Holocene ensemble transient simulations.

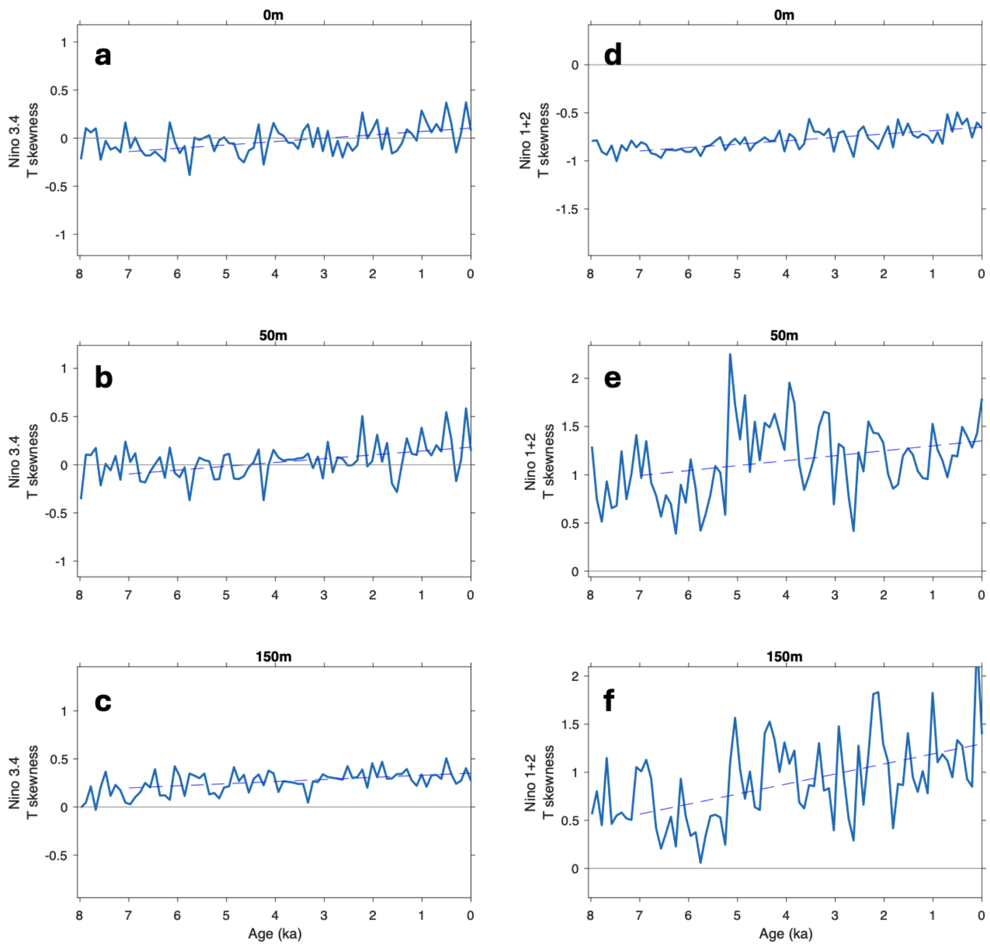

Supplementary Figure 13 | Uncertainty quantification of skewness estimates relative to foraminifera depth habitat. Comparison of (left column) Niño 3.4 and (right column) Niño 1+2 SST (0m) and subsurface temperature (Tsub, at ~50m and ~150m depth) skewness in EC-Earth Holocene transient simulation.

Study	Cores	Location (**Cluster**)	Species	Proxy
Thirumalai et al. 2024	ML1208-21MC/20BB	1°N, 157°W (**CP**)	*Globigerinoides ruber*	$\delta^{18}O$
Glaubke et al. 2024	MV1014-02-17JC & MV1014-02-09MC	0°S, 86°W & 1°S, 85°W (**CP**)	*Neogloboquadrina dutertrei*	Mg/Ca
Grothe et al. 2020; Cobb et al. 2013; 2003; McGregor et al. 2013	–	2-6°N, 162-157°W (**CP**)	Fossil corals	$\delta^{18}O$
Rustic et al. 2020; White et al. 2018	ML1208-17PC & ML1208-14MC1 & ML1208-14MC/12GC	0°N, 156°W & 0°S, 156°W (**CP**)	*Globigerinoides ruber* *Globigerinoides sacculifer*	Mg/Ca
Ford et al. 2015	ODP Site 849	0°N, 111°W (**EP**)	*Trilobatus sacculifer*	Mg/Ca
Carré et al. 2014	–	15-18°S, 104-109°W (**EP**)	*Mesodesma donacium*	$\delta^{18}O$
Sadekov et al. 2013	CD38-17P	1°S, 90°W (EP)	*Neogloboquadrina dutertrei*	Mg/Ca & $\delta^{18}O$
Koutavas & Joanides 2012	V21-30	1°S, 90°W (**EP**)	*Globigerinoides ruber*	$\delta^{18}O$
Leduc et al. 2009	MD02-2529	8°N, 84°W (**EP**)	*Neogloboquadrina dutertrei*	$\delta^{18}O$

Supplementary Table 1

Proxy datasets used in this study. "–" means not applicable.

Model name *Key refs*	**Covered period (ka)**	**Model set-up**			
		Orbital parameters	Greenhouse gases	Vegetation cover	Ice-sheets
TRACE (CCSM3) *Liu et al. 2009; 2014*	22–0	realistic	realistic	dynamic	ICE-5G
EC-Earth3-LR *Zhang et al. 2021*	8–0	realistic	realistic	dynamic	–
IPSL-CM5 *Braconnot et al. 2019*	6–0	realistic	realistic	prescribed	pre-Industrial
MPI-ESM *Dallmeyer et al. 2020; Bader et al. 2020*	8–0	realistic	realistic	dynamic	–
HadCM3-M21d *Hopcroft and Valdes 2021*	10–0	realistic	realistic	dynamic	ICE-6G
LOVECLIM1.3 *Yin et al. 2021*	17–0	realistic	realistic	dynamic	present-day
AWI-ESM2 *Shi et al. 2022*	6–0	realistic	realistic	dynamic	–
CESM1 *Kang and Yang 2023*	6–0	realistic	realistic	dynamic	–
KCM *Segschneider et al. 2018*	9.5-0	realistic	realistic	dynamic	–

Supplementary Table 2

The nine Holocene transient simulations used in this study, and the model set-up. "–" means not considered. The four selected simulations are highlighted in orange.

References

Bader, J., Jungclaus, J., Krivova, N., Lorenz, S., Maycock, A., Raddatz, T., ... & Claussen, M. (2020). Global temperature modes shed light on the Holocene temperature conundrum. *Nature Communications*, 11(1), 4726.

Braconnot, P., Crétat, J., Marti, O., Balkanski, Y., Caubel, A., Cozic, A., ... & Sanogo, S. (2019). Impact of multiscale variability on last 6,000 years Indian and West African monsoon rain. *Geophysical Research Letters*, 46(23), 14021-14029.

Carré, M., Sachs, J. P., Purca, S., Schauer, A. J., Braconnot, P., Falcón, R. A., ... & Lavallée, D. (2014). Holocene history of ENSO variance and asymmetry in the eastern tropical Pacific. *Science*, 345(6200), 1045-1048.

Cobb, K. M., Charles, C. D., Cheng, H., & Edwards, R. L. (2003). El Niño/Southern Oscillation and tropical Pacific climate during the last millennium. *Nature*, 424(6946), 271-276.

Cobb, K. M., Westphal, N., Sayani, H. R., Watson, J. T., Di Lorenzo, E., Cheng, H., ... & Charles, C. D. (2013). Highly variable El Niño–southern oscillation throughout the Holocene. *Science*, 339(6115), 67-70.

Dallmeyer, A., Claussen, M., Lorenz, S. J., Sigl, M., Toohey, M., & Herzschuh, U. (2021). Holocene vegetation transitions and their climatic drivers in MPI-ESM1. 2. *Climate of the Past*, 17(6), 2481-2513.

Ford, H. L., Ravelo, A. C., & Polissar, P. J. (2015). Reduced El Niño–Southern Oscillation during the last glacial maximum. *Science*, 347(6219), 255-258.

Glaubke, R. H., Schmidt, M. W., Hertzberg, J. E., Ward, L. G., Marcantonio, F., Schimmenti, D., & Thirumalai, K. (2024). An inconsistent ENSO response to Northern Hemisphere stadials over the last deglaciation. *Geophysical Research Letters*, 51(12), e2023GL107634.

Grothe, P. R., Cobb, K. M., Liguori, G., Di Lorenzo, E., Capotondi, A., Lu, Y., ... & Toth, L. T. (2020). Enhanced El Niño–Southern oscillation variability in recent decades. *Geophysical Research Letters*, 47(7), e2019GL083906.

Hopcroft, P. O., & Valdes, P. J. (2021). Paleoclimate-conditioning reveals a North Africa land–atmosphere tipping point. *Proceedings of the National Academy of Sciences*, 118(45), e2108783118.

Kang, Y., & Yang, H. (2023). Quantifying effects of Earth orbital parameters and greenhouse gases on mid-Holocene climate. *Climate of the Past*, 19(10), 2013-2026.

Koutavas, A., & Joanides, S. (2012). El Niño–Southern oscillation extrema in the holocene and last glacial maximum. *Paleoceanography*, 27(4).

Leduc, G., Vidal, L., Cartapanis, O., & Bard, E. (2009). Modes of eastern equatorial Pacific thermocline variability: Implications for ENSO dynamics over the last glacial period. *Paleoceanography*, 24(3).

Liu, Z., Otto-Bliesner, B. L., He, F., Brady, E. C., Tomas, R., Clark, P. U., ... & Cheng, J. (2009). Transient simulation of last deglaciation with a new mechanism for Bølling-Allerød warming. *Science*, 325(5938), 310-314.

Liu, Z., Lu, Z., Wen, X., Otto-Bliesner, B. L., Timmermann, A., & Cobb, K. M. (2014). Evolution and forcing mechanisms of El Niño over the past 21,000 years. *Nature*, 515(7528), 550-553.

McGregor, H. V., Fischer, M. J., Gagan, M. K., Fink, D., Phipps, S. J., Wong, H., & Woodroffe, C. D. (2013). A weak El Niño/Southern Oscillation with delayed seasonal growth around 4,300 years ago. *Nature Geoscience*, 6(11), 949-953.

Rustic, G. T., Polissar, P. J., Ravelo, A. C., & White, S. M. (2020). Modulation of late Pleistocene ENSO strength by the tropical Pacific thermocline. *Nature Communications*, 11(1), 5377.

Sadekov, A. Y., Ganeshram, R., Pichevin, L., Berdin, R., McClymont, E., Elderfield, H., & Tudhope, A. W. (2013). Palaeoclimate reconstructions reveal a strong link between El Niño-Southern Oscillation and Tropical Pacific mean state. *Nature communications*, 4(1), 2692.

Segschneider, J., Schneider, B., & Khon, V. (2018). Climate and marine biogeochemistry during the Holocene from transient model simulations. *Biogeosciences*, 15(10), 3243-3266.

Shi, X., Werner, M., Krug, C., Brierley, C. M., Zhao, A., Igbinosa, E., ... & Lohmann, G. (2022). Calendar effects on surface air temperature and precipitation based on model-ensemble equilibrium and transient simulations from PMIP4 and PACMEDY. *Climate of the Past*, 18(5), 1047-1070.

Thirumalai, K., DiNezio, P. N., Partin, J. W., Liu, D., Costa, K., & Jacobel, A. (2024). Future increase in extreme El Niño supported by past glacial changes. *Nature*, 634(8033), 374-380.

White, S. M., Ravelo, A. C., & Polissar, P. J. (2018). Dampened El Niño in the early and mid-Holocene due to insolation-forced warming/deepening of the thermocline. *Geophysical Research Letters*, 45(1), 316-326.

Yin, Q. Z., Wu, Z. P., Berger, A., Goosse, H., & Hodell, D. (2021). Insolation triggered abrupt weakening of Atlantic circulation at the end of interglacials. *Science*, 373(6558), 1035-1040.

Zhang, Q., Berntell, E., Axelsson, J., Chen, J., Han, Z., De Nooijer, W., ... & Yang, S. (2021). Simulating the mid-holocene, last interglacial and mid-pliocene climate with ec-earth3-lr. *Geoscientific Model Development*, 14(2), 1147-1169.